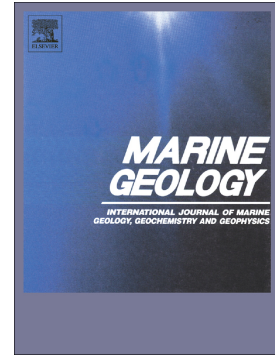


Journal Pre-proof

Late Quaternary tectono-sedimentary processes on an isolated offshore high marginal platform (NW Iberian Continental Margin)

A.E. López-Pérez, B. Rubio, D. Rey, M. Plaza-Morlote, L.M. Pinheiro



PII: S0025-3227(20)30262-0

DOI: <https://doi.org/10.1016/j.margeo.2020.106374>

Reference: MARGO 106374

To appear in: *Marine Geology*

Received date: 7 August 2020

Revised date: 14 October 2020

Accepted date: 17 October 2020

Please cite this article as: A.E. López-Pérez, B. Rubio, D. Rey, et al., Late Quaternary tectono-sedimentary processes on an isolated offshore high marginal platform (NW Iberian Continental Margin), *Marine Geology* (2018), <https://doi.org/10.1016/j.margeo.2020.106374>

This is a PDF file of an article that has undergone enhancements after acceptance, such as the addition of a cover page and metadata, and formatting for readability, but it is not yet the definitive version of record. This version will undergo additional copyediting, typesetting and review before it is published in its final form, but we are providing this version to give early visibility of the article. Please note that, during the production process, errors may be discovered which could affect the content, and all legal disclaimers that apply to the journal pertain.

© 2018 Published by Elsevier.

Late Quaternary tectono-sedimentary processes on an isolated offshore high marginal platform (NW Iberian Continental Margin)

A.E. López-Pérez¹, B. Rubio¹, D. Rey¹, M. Plaza-Morlote¹ and L.M. Pinheiro²

- ¹ Universidade de Vigo. Centro de Investigacións Mariñas (CIM) and Grupo de Xeoloxía Mariña e Ambiental (GEOMA). Campus universitario de Vigo, As Lagoas, Marcosende, 36310, Vigo, Spain.
- ² Department of Geosciences and CESAM, University of Aveiro, Campus de Santiago, 3810-193 Aveiro, Portugal

Highlights

- Surficial sediments are affected by structural features suggesting a tectonic activity still active until recent times.
- Topographic and oceanographic factors induce an intensification of the bottom-hugging currents with their concomitant erosion capacity.
- Erosional activity results in coarser grain-size facies than expected in an offshore source-to-sink sedimentary system.
- A new kind of contourite associated with giant depressions has been defined: the pockmarks-related drift.

ABSTRACT

Studies of the most surficial sedimentary record from passive continental margins provide crucial knowledge about sedimentary dynamics and its changes through recent geological times. These studies allow understanding in detail the influence of both tectonic activity and long-term bottom-current circulation over the Late Quaternary sedimentary dynamics. Using a large dataset of multibeam bathymetry, chirp and multi-channel seismic (MCS) records, ROV seabed direct observations and a magneto-chemical facies characterisation, we provide a well-dated record of the tectono-sedimentary processes on an isolated high marginal platform over the Late Quaternary. Our results display several structural and geomorphological features and tectonic pulses that indicate intense faulting, folding, and deformation of the most recent sedimentary cover. Furthermore, we document four main sedimentary systems acting at the study area and controlled by different water masses (MOW, LSW and NADW): the (hemi)pelagic, bottom current-controlled (hemi)pelagic, contourite and downslope sedimentary systems; as well as a new typology of contourite associated to giant depressions, named as pockmarks-related drift. The record also shows erosive features and extremely low sedimentation rates for the last 172 cal ka BP. Results suggest that the topographic configuration of the high marginal platform and reorganizations of the water masses associated to

climate changes causes a constriction of the water masses that induce an enhancement of the bottom-current activity, favouring erosion, winnowing and redistribution of sediments. Therefore, this study provides new insight into the tectonic control and bottom current activity effect over the Late Quaternary sedimentary cover from an isolated and elevated offshore morphostructural province, located at the Galician Continental Margin.

Keywords: Galician Continental Margin, tectono-sedimentary architecture, bottom current circulation, erosion processes, sedimentary processes, giant depressions

1. Introduction

The recent Late Quaternary sedimentation of passive margins is basically controlled by tectonic, geomorphological, climate and oceanographic factors. Their study brings up essential information about regional geological and environmental evolution such is the case, for example, of the Brazilian Margin (Bezerra et al., 2008; 2020), the West Africa Margin (Séranne and Abeigne, 1999; Séranne and Anka, 2005) or the south-western Adriatic margin (Merdecchio et al., 2007; Pellegrini et al., 2016). Also, the late Quaternary sedimentary record of the passive continental margin of Galicia (NW Iberian Continental Margin) provides an interesting insight into the complex interactions between climate and neotectonic controlling the recent sedimentary infill and geomorphological evolution of this part of the North Atlantic.

The area has attracted numerous studies, which have enhanced global knowledge on deep-marine margin environments and their dynamic evolution over time. Several studies have acquired dataset of seismic profiles, swath bathymetry, and acoustic backscatter data (Montadert et al., 1974; Boillot et al., 1980; Murillas et al., 1990; Pérez-Gussinyé et al., 2003; Reston, 2005; Ercilla et al., 2006; 2008; 2011; Llave et al., 2008; 2018; Medialdea et al., 2008; Vázquez et al., 2008; Jané et al., 2010; Ranero and Pérez-Gussinyé, 2010; Maestro et al., 2013; Dean et al., 2015; Somoza et al., 2019) to characterise the major morphological, tectonic, sedimentary, and oceanographic features. These works provide a good approximation to the dynamic evolution of this margin, particularly on the regional tectonic processes governed by the poly-phase Mesozoic rifting and the Cenozoic compressional regime at the North Atlantic region. They also defined the major stratigraphic sequences and large geomorphological features of the margin. The margin has also been the subject of numerous research focused on how sedimentary and oceanographic processes driven by glacial/interglacial cycles during the Late Pleistocene and Holocene have modelled the main geomorphological features that conformed the present-day submerged landscape of the Galician Continental Margin (Alonso et al., 2008; Rey et al., 2008; Voelker and de Abreu, 2011; Martins et al., 2013; Salgueiro et al., 2014; Hanebuth et al., 2015; Mena et al., 2015; 2018; Zhang et al., 2016; Plaza-Morlote et al., 2017; López Pérez et al., 2019; Petrovic et al., 2019). The sedimentary record is such that permits detailed palaeoclimatic/palaeoceanographic reconstructions of this part of the North Atlantic of global

significance. One remarkable finding is the intensification and deepening (sinking to $\sim 2,000$ m) of the Mediterranean Outflow Water (MOW) during stadials conditions (Voelker et al., 2006; Voelker and de Abreu, 2011), which according to Ercilla et al., (2011) could be related to different erosive and depositional bottom-current features at the study area. During cold stadials also took place the deposition of ice-rafted debris (IRD) caused from the melting of icebergs discharges over North Atlantic (Heinrich, 1988), resulting in a detrital imprint on the sediments of the margin (Alonso et al., 2008; Rey et al., 2008; Martins et al., 2013; Plaza-Morlote et al., 2017; Mena et al., 2018; López Pérez et al., 2019). These works demonstrated that the geographic situation of the Galician Continental Margin makes it a place of interest to study variations of oceanographic and sedimentary conditions associated with climatic changes during the Late Pleistocene and Holocene (Plaza-Morlote et al., 2017). However, the impacts and interactions of the geomorphology and the oceanographic, climate and tectonic regimes over the most surficial sedimentary record have been insufficiently investigated; an aspect that our work dear to investigate from a multidisciplinary perspective.

We have chosen the Transitional Zone morphostructural province because it is an offshore marginal platform characterised by a general elevation of the seafloor in comparison with their adjacent provinces, except at the west where it is limited and flanked by the Galicia Bank province. This confinement condition constitutes a barrier for water masses that could alter the sedimentary dynamics in the area. The occurrence of several giant depression structures (Vázquez et al., 2009b; Ercilla et al., 2011; Druet, 2015; Somoza et al., 2019) and many minor fluid-escape structures related to an intense fluid dynamics (Ribeiro, 2011; Minshull et al., 2020), particularly affecting Late Pleistocene and Holocene sedimentary sequence and subsequently their effect on the local sedimentary dynamics, are aspects that we explore in detail.

Therefore, this paper provides a multidisciplinary approach to the complex interaction between sedimentary systems and oceanographic dynamics and recent tectonic in the isolated high of Transitional Zone morphostructural province. Unlike previously published works, we have combined a large dataset consisting of geophysical and sedimentary records, along with a robust core geochronology reconstruction and direct observations of the seabed. This multiapproach allows obtaining a comprehensive view and characterisation of the uppermost tectono-sedimentary processes and geological and oceanographic evolution of the study area during the past 172 cal ka BP, resolving gaps in the scientific literature and providing a new integrated vision of the sedimentary dynamics and the influence of the bottom current and tectonic over the surficial sediments of an offshore high marginal platform.

2. Regional framework

2.1. Geodynamic and tectonic setting

The West Galician Continental Margin is a non-volcanic passive and hyperextended rifted margin (Boillot et al., 1979; Tucholke et al., 2007) divided into six morphostructural provinces (Murillas et al., 1990; Reston, 2005; Vázquez et al., 2008), named from the continental shelf to the west as the Galicia Interior Basin (GIB), Transitional Zone (TZ), Galician Bank (GB), Northwestern Flank (NF), Deep Galicia Margin (DGM), and Half-Graben Domain (HGD) (Fig. 1a). This physiography evidences a complex tectonic evolution which is the result of the Mesozoic rifting stage and the Cenozoic compressional regimes (Pyrenean orogeny) (Vázquez et al., 2008). The compressional regime is the responsible of the fault pattern of the margin due to the renewing of the Mesozoic faults, observing a decoupling between basement tectonics and the upper sedimentary units that suggest the presence of a viscous layer (Vázquez et al., 2008). Regarding the TZ morphostructural province, it constitutes an area dominated by a horst-graben system, whose basement is compartmentalised in successive blocks bounded by normal faults (Vázquez et al., 2008). In this province have been described two main families of faults: one of these corresponds with the NW-SE to N-S normal faults and the second one is defined by NE-SW transfers faults which show a normal component (Thommeret and Boillot, 1988; Vázquez et al., 2008).

2.2. Morphology and sedimentary systems of the TZ morphostructural province

The study area is the TZ morphostructural province of the West Galician Continental Margin, located between the GIB and GB provinces (Fig. 1b), which correspond to a general elevation of the marginal platform of the Galician Continental Margin (Vázquez et al., 2008). The TZ morphostructural province is characterised by a dome-like morphology located in the centre, which creates an irregular-subrounded sloping seafloor and by a set of several structural highs and scarps (Ercilla et al., 2011; Somoza et al., 2019). The water depths vary from 1,600 to 2,500 m, and this province shows seafloor gradients between $< 0.5^\circ$ and 3° (Ercilla et al., 2011; Somoza et al., 2019). In this area, three giant pothole structures related to the large-scale escape of fluids have been described; the most extensive of them is known as *Gran Burato* or *Burato ERGAP* (Vázquez et al., 2009b; Ercilla et al., 2011; Ribeiro, 2011; Druet, 2015; Somoza et al., 2019; Minshull et al., 2020). The origin of these structures could be related to viscous layer mobility, the “black shale unit” of Albian–Cenomanian age, which was identified as the possible responsible agent for the intense faulting activity in the GB region (Group Galice, 1979; Vázquez et al., 2008; Ercilla et al., 2011).

Ercilla et al., (2011) describes four principal sedimentary processes acting in the TZ morphostructural province: slope apron, contourites (elongated mounded and separated drifts), (hemi)pelagic and mixed systems. The slope apron sedimentary system is characterised by the formation of channelized and/or non-channelized mass movements (mostly mass flows and mass-transport deposits located at the north of the province). The elongated and separated drifts are located surrounding structural highs and scarps, and they are characterised by positive reliefs associated with moats at the foot of the structural

highs and scarps. The (hemi)pelagic system is related to the settled of biogenic and terrigenous components that have fallen through the water column. Interbedded into the sediments, also appear grain-coarse components associated with IRD deposited during Heinrich Events (López Pérez et al., 2019). The mixed system is related to (hemi)pelagic settling under the influence of bottom-current dynamic.

2.3. *Stratigraphy sequence*

The sedimentary cover of the West Galician Continental Margin displays a very irregular distribution over the Palaeozoic basement of the margin. The thickness of the margin is relatively thin, varying from 0 to 7 km (Vázquez et al., 2008). The maximum depocenter of the sedimentary thickness (7 km) is reached in the Galicia Interior Basin; meanwhile, the rest of the morphostructural provinces show a thin sedimentary cover, varying from 0 to 4 km thick (Boillot and Maldonado, 1988; Murillas et al., 1990; Pérez-Gussinyé et al., 2003; Vázquez et al., 2008). The sedimentary sequence mainly fills the extensional Mesozoic basins created over the basement structure, and they comprise ages from the Late Jurassic (Oxfordian) to the present (Murillas et al., 1990; Ercilla et al., 2008; Vázquez et al., 2008).

Seven different seismic units (named from 7 to 1 from oldest to youngest) have been identified along the West Galician Continental Margin defining the seismic stratigraphy of the margin (Murillas et al., 1990; Ercilla et al., 2008). These seven seismic units have been grouped in three different categories attending to their relationship with the structural evolution of the Galician Continental Margin: pre-rift, syn-rift and post-rift seismic unit categories. Thereby, the seismic units 7 and 6 (Oxfordian to Berriasian) comprise the pre-rift seismic units; the seismic units 5 and 4 (Valanginian to Aptian) correspond to the syn-rift seismic units; and the seismic units 3, 2 and 1 (Albian to Quaternary) constitute the post-rift seismic units (Murillas et al., 1990; Ercilla et al., 2008).

2.4. *Oceanographic settings*

The area is under the influence of several water masses (Fig. 1a), the most important of which is the Eastern North Atlantic Central Water (ENACW) that reaches depths of around 650 m, the Mediterranean Outflow Water (MOW) that extend down to around 1,750 m depth, and the Labrador Sea Water (LSW) that extends from 1,500 to 2,200 m depth (Fiúza et al., 1998; Hall and McCave, 2000; McCave and Hall, 2002; Varela et al., 2005; Zhang et al., 2016). Seafloor depths of less than 3,000 m in the TZ and the GIB morphostructural provinces constitute a geomorphological barrier for the deeper water masses of the North Atlantic Deep Water (NADW: 2,150–3,450 m water depth) and the Lower Deep Water (LDW: > 3,450 m water depth) (Bender et al., 2012). The along-slope sedimentary processes acting at the TZ morphostructural province (contourites and mixed system), as well as the erosional features identified, are principally controlled by two water masses: the MOW and the LWS (Ercilla et al., 2011).

3. Dataset and Methods

3.1. Sediment cores and seafloor observations

A total of 13.50 meters of sedimentary record from five piston cores were collected during the *MARBANGA*, *Burato 4240* and *Gran Burato 2011* cruises. The cores, located between 1,644 and 2,827 m of depth, are named as PC13-3, PCL1-2, PC06, PC01, and GC16 (Fig. 1c, d; Table 1). Deep ocean-floor observations were obtained using a Seaeye Cougar 1432 ROV from the ACSM company during the *Gran Burato 2011* cruise. A total of forty-five hours of video records have been obtained from six ROV dives.

3.2. Bathymetric data

Swath bathymetric data were obtained by combining an extended multibeam echosounder dataset acquired during the *MARBANGA* cruise using a Kongsberg Simrad EM120 system onboard the R/V *Hespérides* and during the oceanographic cruises known as *Burato 4240* and *GALINCLIMARCH* using an ATLAS^R Hydrosweep DS onboard the R/V *Sarmiento de Gamboa*. The Kongsberg Simrad EM120 system operates at a frequency of 12 kHz with an operating range from 20 to 11,000 m, whereas the ATLAS^R Hydrosweep DS uses a 15.5 kHz frequency, and its operating range is from 10 to 11,000 m. Multibeam data were processed using the CARISTM and CaribesTM software. Bathymetry for areas without direct data was determined using the EMODnet Digital Terrain Model repository, which for the study area combines the bathymetric data acquired for the Spanish Economic Exclusive Zone (ZEEE) and the General Bathymetric Chart of the Oceans (GEBCO) data. The digital terrain model (DTM) and other derived cartographic products were generated using ArcGISTM and the Global MapperTM software.

3.3. Shallow seismic (chirp) data

About 2,572 km of chirp seismic profiles were obtained (Fig. 1b, c, d) using a TOPAS (TOPographic PArametric Sonar) PS 12 system during *MARBANGA* cruise onboard the R/V *Hespérides*, and a parametric sub-bottom profiler atlas Parasound P35 during *Burato 4240* cruise onboard the R/V *Sarmiento de Gamboa*. Furthermore, the shallow seismic dataset was acquired using a 3.5 kHz CHIRP system on board of the RV *L'Atalante* during *ERGAP* cruises. The penetration of the acoustic signal using these systems varies between 0 and 160 milliseconds (TWT). Chirp seismic data were processed (static correction to correct vertical shift, kill trace command, Butterworth filtering and burst noise removal filters, Stolt F-K migration, F-X deconvolution filtering, and muting were used for reducing noise and enhanced seismic data) using the RadeproTM software. The resulting SEG-Y files were imported into the Kingdom SuiteTM software for interpretation. For the echo-character analyses and the nomenclature used, the methodologies established in the classical works of Damuth, (1980) and Pratson and Laine, (1989) were taken into account and adapted to the acoustic response of

the study area (Llave et al., 2018; Maestro et al., 2018a). The correlation of the echo-character data with the detailed bathymetric data obtained from the multibeam echosounder was used for the interpretation and discussion of the sedimentary and oceanographic processes.

3.4. Multi-channel seismic (MCS) data

The MCS profiles were acquired during the *Burato 4240* cruise (Fig. 1c). The seismic source was composed of an array of 10 airguns shooting every 50 m, and the streamer was 2,243 m in length and composed of 156 channels. Multi-channel seismic profiles were processed and interpreted using the Radepro™ and Kingdom Suite™ software. The penetration of the acoustic signal was about < 2 s (TWT).

3.5. Geochemical and sedimentary analyses

High-resolution XRF geochemical and magnetic susceptibility (χ) data, as well as optical and radiographic images of piston cores, were measured with the Itrax™ Core Scanner at the University of Vigo, operated with a Mo-tube with a voltage of 30 kV and an exposure time of 20 s. Semi-quantitative high-resolution XRF geochemical raw data (1 mm step size) were smoothed using a 10-points running mean (1 cm) (Rodríguez-Germade et al., 2013). Grey levels (GL) and RGB values were exported from radiographic and optical images, respectively.

Total inorganic carbon (TIC) content was measured every 2 cm for the first metre and a half of each core and every 4 cm for the remaining core using the elemental macro analyser LECO CNS-2000 of the University of Vigo. CaCO_3 percentages were estimated using the equation $\text{TIC} \times 100/12$, where 100/12 is the molecular weight ratio of CaCO_3 to carbon (Plaza-Morlote et al., 2017).

Grain-size distributions were determined from discrete samples collected every 2 cm for the first metre and a half and every 4 cm for the remaining core using a laser diffraction particle size analyser, the Coulter LS 13 320 (Beckman Coulter Inc., Brea, CA) from the University of Vigo.

Carbon and oxygen stable isotope analyses were performed on two facies of core GC16 at 8.5 and 19.5 cm of depth to characterise the composition and the possible methanogenic origin of the carbonates. The measurements were carried out on the bulk fraction and the matrix fraction ($< 4 \mu\text{m}$) using a GasBench II system coupled to a DELTA V Advantage isotope ratio mass spectrometer (IRMS) at the Autonomous University of Madrid.

The mineralogy and the sedimentary textures of the cores were studied by a JEOL JSM-6700f scanning electron microscope (SEM) operated in backscattering mode (BS), located at the University of Vigo.

The statistical facies analyses were carried out using the SPSS package v.23 with the methodology proposed by López Pérez et al. (2019). In order to get a reliable facies classification of the cores,

different multivariate statistical analyses (Cluster Analysis and Discriminant Analysis) were applied in a large high-resolution geochemical, magnetic and sedimentological dataset. Furthermore, mean grain size (MGS) and sorting allowed defined textural parameters for each core.

3.6. Core chronology

The age models are based on seventeen radiocarbon dating (^{14}C) and their correlation to the nearby cores MD95-2039 and MD95-2040 (de Abreu et al., 2003; Schönfeld et al., 2003). The age models of these cores are based on ^{14}C dates, $\delta^{18}\text{O}$ stratigraphy and SST GISP2 synchronisation. For that, in order to convert the MD95-2040 ages derived from Greenland Ice Sheet Project 2 (GISP2) to Greenland Ice Core Chronology 2005 (GICC05) ages we used the methodology proposed by Stríkis et al. (2018) until 104 ka. All the cores were synchronised by tuning their CaCO_3 or XRF-Ca records (Thomson et al., 1999) (Supplementary data I).

Sixteen monospecific handpicked samples of the planktonic foraminifera *Globigerina bulloides* (two samples from core PC13-3, two from PCL1-2, three from PC06, five from PC01, and four from GC16) and one pteropod samples (from core PC01 at 1635 cm depth) were analysed for radiocarbon dating by accelerator mass spectrometry (AMS). The ^{14}C ages were converted to calendar ages (Supplementary data I) using the IntCal13 calibration curve (Reimer et al., 2013), including a constant 400 yr reservoir correction (Plaza-Morlote et al., 2017).

The age models were developed using a stratigraphy-based Bayesian approach running the OxCal software v4.3.2 (Supplementary data II) (Ramsey, 2008; 2017) to produce a statistically robust age model for each core.

4. Results

4.1. Classification, characterisation, and distribution of echo-characters

The combination of the chirp seismic profiles and bathymetric data allowed us to identify, interpret, and map ten high-frequency echo-character types within the study area (Fig. 2; Table 2). These echo-characters have been grouped into three main classes: distinct echoes (1A, 1B, 1C, 1D, 1E, 1F, and 1G), wavy echoes (2A), and hyperbolic echoes (3A and 3B) (Fig.2; Table 2).

4.1.1. Echo type 1A

This type is defined as continuous and distinct sharp bottom echoes with absent or extremely weak sub-bottom reflectors, and it extends about 3,329.46 km² (Fig. 2; Table 2). This echo type extends partially surrounding the Ordoño and Málaga highs and over the steep-flank located at the northwest of the study area (Fig. 2). Also, it is distributed over the slopes that connect the TZ and GIB morphostructural provinces, as well as over the moats identified surrounding structural highs or scarps (Fig. 2).

4.1.2. *Echo type 1B*

This type is defined by continuous and distinct sharp bottom echoes, with sharp parallel and stratified sub-bottom reflectors (Table 2). The 1B echo-character is the most extensive, covering approximately 5,474.94 km² (Fig. 2), and it appears in low-slope surfaces in the entire study area (Figs. 2, 3b).

4.1.3. *Echo type 1C*

This type shows distinct sharp bottom echoes, and erosional bottom surfaces with undulated, truncated and parallel sub-bottom reflectors, and it covers about 953.49 km² (Fig. 2; Table 2). The 1C echo type is located at the maximum surface elevations identified in the study area (Figs. 2, 3a), as well as at the edge of the east scarps, the top of the *Fernando* high and partially surrounding the *Fernando*, *Sancho*, *Barcelona*, and *Savoie* structural highs (Fig. 2)

4.1.4. *Echo type 1D*

This type is characterised by distinct sharp bottom echoes with inclined, truncated and stratified sub-bottom reflectors, and it occupies an area of around 1,881.78 km² (Fig. 2; Table 2). This type extends mainly surrounding the northern and eastern areas of the mentioned maximum surface elevations (Figs. 2, 3a).

4.1.5. *Echo type 1E*

This echo-character type is identified by distinct weak and erosive bottom echoes and truncated and parallel sub-bottom reflectors, which cover an area of approximately 530.90 km² (Fig. 2; Table 2). The 1E echo type appears over the channels and troughs systems identified (Fig. 2).

4.1.6. *Echo type 1F*

This echo type is defined by continuous and distinct sharp bottom echoes with undulated, parallel, truncated, discordant, and outcropping sub-bottom reflectors. It characterises a surface area of about 110.86 km² (Fig. 2; Table 2). The 1F echo type covers the maximum surface elevation located at the southeast of the *Gran Burato* and *Crater 3* depressions (Fig. 2).

4.1.7. *Echo type 1G*

Echo type 1G characterises weak distinct bottom echoes with high-reflectivity sedimentary layers on an irregular and not defined base (Table 2). This type occupies an area of about 97.41 km², and it is located at the mouth of a drainage channel system associated with the base of the scarps of the GB morphostructural province, which flow toward the east (Fig. 2).

4.1.8. *Echo type 2A*

This echo-character comprises wavy irregular bottom echoes with transparent fill over an irregular base in the first several metres of depth, followed by intermittent transparent layers and parallel, undulated, and discontinuous sub-bottom reflectors not concordant with the seafloor (Table 2). This echo type covers an area of about 479.24 km² located on the surface of the GB plateau at the GB province (Fig. 2).

4.1.9. *Echo type 3A*

The 3A echo type shows distinct sharp echo bottoms with irregular and overlapping hyperbolas without sub-bottom reflectors (Table 2). This echo type extends around 2,834.57 km² (Fig. 2). This echo type is distributed over high-slope surfaces throughout the entire study area (Fig. 3b), coincident with high-slope channels, gullies, troughs, scarps, and structural highs (Fig. 2).

4.1.10. *Echo type 3B*

The 3B echo type is characterised by irregular overlapping hyperbolas with truncated, concordant, or absent sub-bottom reflectors and it has an area of about 498.62 km² (Fig. 2; Table 2). This echo type is located over the channels and scarps mapped in the HCD morphostructural province (Fig. 2).

4.2. Physiography and geomorphological features

The TZ morphostructural province constitutes a NW–SE-elongated province that is characterised, in general terms, by slopes of about 0.5 to 2.5° (Fig. 3a, b) and depths between about 1,500 m and 3,000 m, reaching 5,000 m at the northern boundary (Figs. 3a, 4). The extension and the boundaries of this morphostructural province are delimited in Fig. 4. Geomorphologically, the TZ morphostructural province constitutes an offshore high marginal platform that could be divided into two well-differentiated geomorphological areas: the flat north sector and the elevated south sector (Fig. 3a, c). The north sector is located between the latitudes of 42°50'N and 43°29'N and is characterised by a maximum width of ~ 75 km. This sector constitutes a relatively flat surface (Fig. 3a, c) with depths increasing toward the north, approximately from 2,050 m to 3,000 m, except the northeast area that descends to 5,000 m (Figs. 3a, 4). In contrast, the south sector is located approximately 42°05'N and 42°50'N, and it shows a maximum width of ~ 105 km. Depths in this sector vary approximately between 1,500 m and 2,750 m (Figs. 3a, 4). The south sector is characterised by showing a general topographic uplift of the area compared with its surrounding (Fig. 3c). Here, it is possible to identify three maximum surface elevations, resulting in a dome-like configuration that is the main feature that allows differentiating the south and north sectors (Fig. 3a, c).

Within the study area, different geomorphological features were identified: faults, fold bulges, structural highs, scarps, giant depressions, structural undulations, gullies, troughs, channels, drifts, moats and sediment waves (Figs. 4, 5, 6).

4.2.1. Faults

Faults have been identified from the bathymetric record and seismic data throughout the study area. Bathymetrically, faults are associated with bathymetric lows and morphological lineament structures such as troughs and structural undulations (Figs. 4, 5a, d, f). Faults have also been widely identified in chirp data, folding and deforming the sedimentary record (Figs. 7, 8, 9). These faults show continuity and correlate in terms of depth with the identified faults in MCS profiles (Fig. 7g). Furthermore, MCS data exhibit a large numbering of normal faults affecting the uppermost sediments with an offset of ~ 10 ms TWT (Figs. 6, 7g, 10), confirming the structural control of the troughs and structural undulations (Fig. 10).

In general terms, bathymetric lows and morphological lineaments (e.i., troughs and structural undulations) associated with faults display main NW-SE orientation and a variable surface rupture length between 1 to <15 km (Fig. 4). These faults exhibit a vertical to sub-vertical dip in the shallow sedimentary records (Figs. 7, 8, 9), and they present an offset at the current seafloor from few several meters to < ~ 90 m (Fig. 5a, d, f).

4.2.2. Fold bulges

Three different fold bulges have been identified at the south sector of the marginal platform from bathymetry, and chirp and MCS seismic data, numbering from 1 to 3 from west to east (Figs. 4, 5c, h, 10). These positive seafloor flexures are coincident with the three principal maximum surface elevations of the dome-like structure (Fig. 3a). Fold bulges 1 and 2 have mainly N-S to NNE-SSW orientations; whereas fold bulge 3 displays an NW-SE orientation (Figs. 4, 5h), showing longitudes between 7 and 15 km related to their morphological expression over the seafloor (Fig. 4). These positive flexures are located within the 1C echo type (Fig. 2; Table 2). Regarding MCS data, Fig. 10a, b displays anticlines structures that deform the sedimentary cover, which is strongly affected by normal faults. These anticlines cause the fold bulges described (Fig. 10) corresponding to the maximum elevations within the dome-like structure located at the south sector (Fig. 3a, 4, 5c, h).

4.2.3. Structural highs

Six structural highs were identified within the TZ morphostructural province (Figs. 4, 5h). The *Sancho*, *Savoye*, and *Barcelona* highs, with minimum depths of 1,100 m, 1,370 m, and 1,400 m respectively, are located in the south sector; meanwhile, the *Ordoño*, *Fernando*, and *A* highs, with depths of 1,500 m, 2,040 m, and 2,330 m respectively, are in the north sector (for more details about geological descriptions, see Vanney et al., 1979; Ercilla et al., 2006; 2011; Somoza et al., 2019). These structural highs are mainly delimited by scarps (except the *Barcelona* and *Ordoño* highs) and widely surrounded by moats (Fig. 4), and they are characterised by the echo type 3A (Fig. 2; Table 2). Only Fernando high shows the 1C echo type covering the tabular top (Fig. 2; Table 2).

4.2.4. Scarps

Scarps mainly constitute the boundaries with the adjacent morphostructural provinces (Fig. 4). This is the case of the east boundary between TZ and GIB morphostructural provinces and the west and north boundaries with HGD, GB and NF provinces (Fig. 4, 5b). Scarps also are located surrounding structural highs such as Sancho, Savoye, Malaga, Fernando and A highs (Fig. 4). These scarps display variable orientations (NW-SE, N-S, NE-SW and W-E) and lengths between ~ 4.5 and ~ 81.3 km (Fig. 4). The reliefs vary between ~ 100 and $\sim 2,150$ m and the hyperbolic 3A and 3B echo types characterise these morphological features (Fig. 2; Table 2).

4.2.5. Giant Depressions

Our bathymetric and seismic data confirm the presence of three giant depressions of kilometre diameter located at the southern elevated topographic area of the TZ morphostructural province, which they were already previously reported in the scientific literature (Vázquez et al., 2009b; Ercilla et al., 2011; Ribeiro, 2011; Druet, 2015; Somoza et al., 2019; Minshull et al., 2020): the *Gran Burato*, *Crater 3* and *A Orella* depressions (Figs. 4, 5h, 6).

The *Gran Burato* depression is located at the top of the dome-like morphology, specifically east of the fold bulge 2 (Figs. 4, 5h, 6). This depression has a circular shape with a fairly flat floor bottom, and it displays a size of about 9.56 km^2 (Fig. 6). Also, the maximum and minimum water depths of this depression are 1,975 and 1,607 m, respectively. The *Gran Burato* depression has a maximum W–E and N–S diameters of about 3.4 km and a depth of roughly 367.5 m relative to the surrounding seafloor (Fig. 6). This structure is characterised by a conical morphology and a radially symmetrical depression (Fig. 6), with the west and northwest flanks more topographically elevated compared with the east and southeast flanks, as a result of the surface elevation of the NNE–SSW-oriented fold bulge 2 (Figs. 4, 5h, 6). The flanks display a mean slope of 8.37° , reaching maximums between 20° and 23° (Fig. 3b). *Gran Burato* depression is within the 1C echo type (Fig. 2; Table 2). Regarding seismic data, MCS profiles exhibit truncated reflectors in the flanks of the *Gran Burato* structure, and the absence of internal filling sediments inside the depression (Fig. 6). It is also possible observed intense faulting, caused by normal faults dipping towards the centre of the depression structure (Fig. 6). These faults have an offset of around 10 ms TWT. In the surrounding *Gran Burato* area, chirp record exhibit parallel and undulated reflectors strongly affected by faults and deformations, as well as truncated reflectors (Tr) over the *Gran Burato* flanks (Fig. 9) and the surrounding seafloor (Figs. 7a, 9).

The *Crater 3* displays irregular shape in plan view and an area of 8 km^2 (Figs. 4, 5h, 6). The maximum and minimum water depths of *Crater 3* are 1,850 and 1,775 m respectively. This depression shows a maximum W–E and N–S diameters of about 3.07 and 3.11 km respectively and relative depth of about 77.98 m (Fig. 6). The structure has no symmetry, and the seafloor of the depression is flat with a gentle slope to the east (Figs. 3b, 6). It is also possible to differentiate positive

and negative reliefs at the seafloor with an NW–SE orientation (Figs. 6). The flanks show an average slope of 2.49° with maximums around 5° and 7° (Fig. 3b), and the structure is also within the 1C echo type (Fig. 2; Table 2). In the MCS data, the *Crater 3* displays stratified and parallel reflectors with truncated termination over the palaeoflanks and intense normal faulting (offsets about 10 ms TWT) (Fig. 6). Normal faults also display an inclined distribution towards the centre of the structure. Internally, the depression shows sedimentary filling with a maximum thickness of 110 ms TWT, which also display onlap terminations over the palaeoflanks (Fig. 6). Two fill sediment units have been identified based on the presence of toplap between the lower and upper units (referred as C2 and C1, respectively), with maximum thicknesses of 60 ms TWT and 50 ms TWT, respectively (Fig. 6). This structure shows gentle slopes in contrast to the other two giant depressions identified (Fig. 6).

The *Orella* depression has elliptical shape morphology in plan view and a total area of around 14.39 km² (Figs. 4, 5h, 6). The depression is located between water depths of 2,040 and 1,840 m, and it has maximum W–E, and N–S diameters are 4.78 km and 3.68 km, respectively; the maximum relative depth is 196.74 m (Fig. 6). The *Orella* has a W–E mirrored symmetry, being the west and north flanks are more elevated compared to the east and south ones (Fig. 6). Furthermore, three negative reliefs have been identified from north to south at the seafloor of this structure (Fig. 6). These lows delimit by two positive reliefs and the flanks of the depression. Southernmost of these two positive reliefs show a convex and crescent shape; meanwhile, the northernmost positive relief has a west-east elliptical shape (Fig. 6). The flanks show an average slope of about 4.42° with maximum slope values between 10° and 15° (Fig. 3b), and the *Orella* depression is also characterised by the 1C echo type (Fig. 2; Table 2). Furthermore, the *Orella* depression shows in MCS profiles truncated terminations of the parallel and stratified reflectors over the palaeoflanks, as well as normal faults inclined toward to the centre of the structure (offsets about 10ms TWT) (Fig. 6). This depression has a filling of sediments of maximum thickness of 226 ms TWT (Fig. 6). The fill is characterised by internal reflectors with onlap termination over the palaeoflanks of the depression. Three different fill units have been identified based on the toplap and downlap terminations over the reflectors that limit these units (Fig. 6). The lower unit, named as O3, is characterised mainly by inclined reflectors to the south with toplap, downlap and onlap terminations and local chaotic reflectors, especially in the N–S profile, and it has a thickness around 112 ms TWT (Fig. 6). The intermediate unit, labelled as O2, shows mainly parallel and stratified reflectors with some located toplap and downlap terminations between internal reflectors; the thickness of this unit is about 85 ms TWT (Fig. 6). Finally, the upper unit, named as O1, exhibits parallel and stratified reflectors, and it has a thickness of about 29 ms TWT (Fig. 6). Furthermore, truncated reflectors appear in this unit over the seafloor surface corresponding to the slopes of positive and negative reliefs (Fig. 6).

4.2.6. Structural undulations

Bathymetric lows associated to structural undulations are found along the whole area, especially at the west and south of the *Gran Burato* depression and in the centre and eastern regions of the north sector (Figs. 4, 5d, h). These structural undulations are mainly oriented NW–SE and they have sinuous lengths from 1 to 9 km, with around 0.5 to 2.5 km between crests and negative reliefs from several few meters until $< \sim 50$ m (Figs. 4, 5d). Structural undulations are mainly within the 1B echo type, but also are present within the 1C, 1D and 1F echo types (Fig. 2; Table 2). Furthermore, from chirp and MCS data, it is possible observed that faults govern the structural undulations features (Figs. 7a, b, f, 10b), folding the sedimentary record.

4.2.7. Gullies, troughs and channels

Different erosional features associated with gullies, troughs and channels have been identified within this high marginal platform (Figs. 4, 5e, f, g, h). Numerous gullies are located at the sharp northeast boundary, extending toward the GIB morphostructural province with a NE-SW trend (Fig. 4, 5e). In less extend, gullies also appear at the boundary with the FGD morphostructural province with an NNE-SSW orientation (Fig. 4). These features display V-shape morphology with an around one to several kilometres width. The lengths are about 2-5 km, and the relief is less of ~ 250 m (generally about several tens of meters) (Fig. 4, 5e). Furthermore, gullies are characterised by the 3A echo type, showing hyperbolic facies (Fig. 2; Table 2).

Bathymetric lows, associated with structural troughs, have been identified at the domo-like structure located at the south sector of the marginal platform (Figs. 4, 5f, h). These troughs flow to the east and northwest from the area north of the *Gran Furato* depression, and they have an NW-SE trend (Fig. 4). The lows display U-shape morphology, and they have a length less of 15 km and a wide of around between ~ 1 -2 kilometres, with relief $< \sim 90$ m (Fig. 4, 5f). Furthermore, troughs are characterised by the 1E and 3A echo types (Fig. 2; Table 2). These geomorphological features have a structural control because normal faults govern them as the seismic analysis confirms in chirp and MCS data (Figs. 9, 10b). These normal faults flank the structural troughs and deform the surficial and deep sediments (Figs. 9, 10b). Chirp and MSC data exhibit truncated reflectors over the structural troughs (Figs. 9, 10b; Table 2), as well as hyperbolic facies (Fig. 9; Table 2).

Regarding channels, different systems have been identified within the study area (Figs. 4, 5g, h). These channels develop seaward from the slope break of the scarps, or they represent the thalweg incision of structural valleys, following in both cases, the maximum slope gradient (Fig. 4). One of these systems is located at the base of the scarps of the GB morphostructural province at the west of the north sector of the TZ morphostructural province (Figs. 4, 5g, h). These channels represent a drainage system with a mainly SW-NE orientation, and they have lengths of roughly 10–22 km; the largest is about 36 km in length (Figs. 4, 5g, h). Moreover, a channel system roughly 25–34 km in length descends with SW-NE/SSW-NNE trend from the *Fernando* and *A* structural highs, and it

connects the TZ morphostructural province with the Biscay Abyssal Plain, reaching its maximum depth (Fig. 4). Finally, another extensive channel system of about 33 km in length descends southwest forward from GB and TZ provinces towards the HGD province (Fig. 4). In general terms, channels display U and V-shape morphologies of < 2 km of wider, with reliefs that vary between few meters to < ~ 180 m (Figs, 4, 5g). These erosional features are coincident with the 1E, 3A and 3B echo types (Fig. 2; Table 2). Chirp profiles display truncated reflector over the flanks of the channels (Fig. 7d; Table 2), as well as hyperbolic facies (Table 2)

4.2.8. Drifts and moats

Different elongated mounded and separated drifts have been identified in the study area as positive reliefs associated parallel with the *Barcelona*, *Sancho*, and *Savoie* highs, as well as with the base of the scarps of the GB morphostructural province (Figs. 4, 5b). These drifts are separated from the structural highs and scarps by moats (Figs. 4, 5b). These structures are located between 1,500 and 2,000 water depth, and they have reliefs of ~ 10 to < ~ 160 m and a wide between ~ 3 and ~ 6.5 km. Drifts are located within the 1B echo type (Fig. 2; Table 2). Chirp data displays stratified reflectors characterising drift deposits (Fig. 7a).

Regarding moats, these erosional features are located surrounded almost all structural highs (the *Savoie*, *Sancho*, *Barcelona*, *GB*, *Málaga*, *Cadoño*, *Fernando* and *A* highs) and some scarps (Figs. 4, 5b). Moats comprise between 4 and 35 km of length and a few kilometres, or less, of wide. Cross-sections have U-shape morphology, and reliefs vary between several tens or hundreds of meters (< ~ 350 m). Moats are associated with the 1A echo type (Fig. 2; Table 2). Chirp profiles show transparent facies associated with the moats (Fig. 7a).

4.2.9. Sediment waves

Finally, sediment waves have been identified from chirp seismic analysis at the top of the plateau of the GB province (Fig. 4) associated with the 2A echo type (Fig. 2; Table 2). These features are located at ~ 700 and ~ 900 m of water depths and show amplitude < 8 m and a wavelength of several hundred meters.

4.3. Chirp seismic analysis

4.3.1. Seismic unit analysis

Interpretation of the chirp seismic profiles, acquired mainly in the uplifted south sector of the TZ morphostructural province (Fig. 1b, c, d), allowed us to identify three different seismic units with a patchy distribution around this area (Fig. 7). These seismic units are named U3 to U1 from older to younger. The criteria established to define the seismic units were based into several factors: a) the appearance of high amplitude and continuity reflectors along the seismic lines (Fig 7), b) the

recognition of onlap internal reflectors terminations against these high amplitude reflectors identified (Fig. 7b), and c) the correlation of the high amplitude and continuity reflectors between the different seismic profiles, maintaining the thicknesses of each seismic unit at each correlation.

Units U3 to U1 exhibit mainly the 1B acoustic facies, and they are characterised by showing parallel and undulated reflectors with alternation of high and low amplitudes (Fig. 7). These units are principally distributed at the western and southern areas of the three fold bulges (Fig. 7a, b). In contrast, at the three maximum surface elevations coincident with the fold bulges described, these three units are thinner, and chirp profiles show truncated reflectors with the seafloor surface corresponding to the 1C and 1D acoustic facies, defining erosional surfaces (Figs. 7a, b, 8; Table 2). These truncated reflectors are also recognizable in MSC profiles (Fig. 10). In these areas, seismic units also display internal onlap terminations (Fig. 7b). The three younger seismic units are strongly affected by the structural undulations and normal faults that deform the units and cause changes in their thickness (Fig. 7a, b, e, f), varying between maximums and minimums around 8 and 2 ms TWT, 26 and 4 ms TWT, and 19 and 6 ms TWT for units U1, U2, and U3 respectively.

Additionally, at the NE of seismic line L (Fig. 7b) the lower limit of Unit 1 could be correlated with core PC13-3 at approximately ~ 3.40 m (~ 4.5 ms TWT), coincident with an abrupt change in grain size (Fig. 7c). From this depth, there is a substantial decrease in the sand content of the core (Fig. 7c).

4.3.2. Seismic structure analysis

Structural deformations and pockmark structures have been identified from chirp records affecting the units described (Figs. 7b, e, f, 8, 9).

Fig. 7 displays transparent bodies without stratigraphic correlation that intercept the seismic units and inducing local discontinuities and truncated reflectors. These structures correspond to structural deformations resulting from the intense fault activity observed in the chirp seismic profiles (Fig. 7b, e, f). Structural deformations are also related in terms of depth with the erosional surfaces define by the 1C and 1D echo types (Fig. 2; Table 2) coincident with the highest topographic surfaces of the south sector (Fig. 7a, b) and with the structural undulations affecting the stratified surficial deposits (Fig. 7f). Filled and partially filled pockmarks have been identified in chirp seismic profiles (Figs. 8, 9). These pockmarks are characterised by presenting undulated reflectors with V-morphologies delimited by faults (Fig. 8), and they are associated with gravitational collapses due to fluid leakages (Llave et al., 2018). The filled and partially filled pockmarks are chiefly distributed at the uplifted areas resulting in the fold bulges 2 and 3, especially within the 1F acoustic facies (Figs. 2, 8; Table 2), although some pockmarks have been identified within 1C acoustic facies surrounding the *Gran Burato* depression (Fig. 9). Furthermore, Fig. 8a shows an unfilled pockmark. Finally, filled pockmarks have also been recognised in MCS profiles (Fig. 10a),

4.5. ROV observations

Six ROV dives allowed filming the seafloor of the *Gran Burato* structure and the troughs system located at the northeast of this depression (Fig. 11). ROV video visualisations enabled us to identify the following sedimentary features:

- a) Ripples with rectilinear crests, some of them with an accumulation of pteropods into the lows between crests (Fig. 11a). These features are located mainly at the bottom of the depression and the southern area of the troughs system (dives 5, 6 and 10).
- b) Grooves with or without observed accumulations of pteropods in the inner part of the depression and in the south area of the troughs system (dives 6 and 10) (Fig. 11b).
- c) Comet marks associated with rock fragment trails that are aligning with the direction of the current behind an obstacle (dives 2, 6, 7, 8 and 10) (Fig. 11c).
- d) Dense crusts located principally at the flanks of the depression and in the southern area of the troughs (dives 2, 5, 6 and 10) (Fig. 11d). These dense crusts display laminated morphology, and they are partially covered by sands (Fig. 11d).
- e) Flat surfaces without ripples, with some dispersed mounds and, rarely, some holes (mainly identified in dives 6, 7 and 8) (Fig. 11e). These flat surfaces could be appearing covered by pteropods and/or ferruginous tubes, especially in dive 6 (Fig. 11f).

4.6. Sediment core data

4.6.1. General sediment properties

In general terms, the sediments texture of cores PC13-3, PCL1-2, PC06, and GC16 consist of well-laminated very poorly sorted fine to very fine sand, except core PC01, which is dominated by very poorly sorted medium sand (Table 3). Mean RGB colour values indicate sienna tones for cores PC13-3 (231, 209, 170) and PCL1-2 (215, 184, 125) and light brown and olive tones for cores PC06 (161, 149, 113), PC01 (150, 135, 95), and GC16 (161, 144, 110). Only the bottom of core GC16 shows a pale brown colour (194, 176, 143) different from the rest of the cores.

4.6.2. Facies analysis

Multivariate statistical analyses have been applied to the geochemical (XRF: Fe, Ti, Ca, Mn, and Ba; XRF: Fe/Ca, Ti/Ca, and Si/Sr detrital ratios), sedimentological (grain-size, grey level, and RGB colour), and magnetic (MS) data for the facies classification of the five piston cores extracted from the TZ morphostructural province. The analyses were carried out using the methodology by López Pérez et al. (2019). Exploratory cluster analysis (CA) was performed on the dataset to define the preliminary facies classification. These CA results were improved and refined using discriminant analysis (DA) to obtain a final facies classification that shows the robust statistical agreement of 85.9%, 87.5%, 94.5%, 99.3%, and 100% for cores PC13-3, PCL1-2, PC06, PC01, and GC16 respectively. Furthermore, low

values of Wilks's lambda (PC13-3 = 0.180, PCL1-2 = 0.260, PC06 = 0.104, PC01 = 0.027, and GC16 = 0.030), together with the high chi-square values (PC13-3 = 6,940.41, PCL1-2 = 4,615.24, PC06 = 7,287.08, PC01 = 6,153.21, and GC16 = 741.93), ensured the validity of the facies classification results ($p < 0.0001$). At the same time, SEM observations provided additional information on the sedimentary texture and mineralogy of each facies.

A total of seven different textural and magnetochemical facies were defined for all the cores (Figs. 12, 13; Table 4). Statistical analyses of the datasets corresponding to cores PC13-3, PCL1, and PC06 revealed three different main facies: Ca-rich low-susceptibility/pelagic (Fig. 13a, b), Fe-rich high-susceptibility/detrital (Fig. 13c), and medium Ca and Fe/hemipelagic facies (Fig. 13d). Core PC01, extracted from the bottom of the *Gran Burato* depression, shows three facies from the top to the bottom of the core: a foraminifera-rich sand facies (Fig. 13e), a pteropod-rich sand facies (Fig. 13f), and a detrital facies (Fig. 12). Core GC16, extracted from the trough system located at the northeast of the *Gran Burato* structure, exhibits two very different main facies: a low-density sand facies (Fig. 13g) at the top of the core and a high-density silt facies (Fig. 13h) at the bottom of the core. The boundaries of these facies are coincident with changes in the RGB colour and GL profiles (Fig. 12; Table 4).

4.6.3. Stable isotope analyses

Oxygen and carbon stable isotope analyses were carried out on the bulk carbonate fractions and matrix carbonate fractions ($< 4 \mu\text{m}$) of the *Low-den sand* and *High-den silt* facies identified in core GC16 (Fig. 12). Results from the $\delta^{13}\text{C}$ and $\delta^{18}\text{O}$ isotopic compositions for the bulk and cement carbonate fractions of the low-density facies ($\delta^{13}\text{C}_{\text{bulk}} = 0.05\text{‰}$, $\delta^{13}\text{C}_{\text{cement}} = 0.73\text{‰}$, $\delta^{18}\text{O}_{\text{bulk}} = 1.04\text{‰}$, and $\delta^{18}\text{O}_{\text{cement}} = 1.09\text{‰}$) and the high-density facies ($\delta^{13}\text{C}_{\text{bulk}} = 0.37\text{‰}$, $\delta^{13}\text{C}_{\text{cement}} = 0.91\text{‰}$, $\delta^{18}\text{O}_{\text{bulk}} = 1.24\text{‰}$, and $\delta^{18}\text{O}_{\text{cement}} = 1.94\text{‰}$), reflect marine carbonate isotopic conditions (Joseph et al., 2013).

4.6.4. Sedimentation rate.

In general terms, sedimentation rates of cores PC13-3, PCL1-2, and PC06 showed extremely low values corresponding to the cold stadials, with average values of 2.73 cm ky^{-1} , 1.34 cm ky^{-1} , and 0.49 cm ky^{-1} corresponding to MIS 2, MIS 3, and MIS 4 respectively, with minimums values between 0.02 and 0.34 cm ky^{-1} (Fig. 14). MIS 1 showed a mean value of 1.85 cm ky^{-1} , and the warm MIS 5 period had a mean rate of 7.55 cm ky^{-1} , with maximums ranging between 16.95 and 13.36 cm ky^{-1} (Fig. 14). MIS 6 displayed a mean value of 5.45 cm ky^{-1} with maximums and minimums of 11.26 cm ky^{-1} and 0.02 cm ky^{-1} respectively. During this stage, the lowest sedimentation rates were calculated between 155 and 140 cal ka BP, defining a hiatus located at $\sim 3.40 \text{ cm}$ of the core PC13-3; meanwhile, the higher values were obtained from 172 to 155 cal ka BP (Fig. 14). Furthermore, the general low sedimentation rates caused a condensed sequence of detrital layers in cores PC13-3, PCL1-2 and PC06 (Fig. 12). Note that PC06 show the higher sedimentation rates of the three cores (Fig. 14).

Core GC16 displayed very low sedimentation rates for the last 30 cal ka BP (mean of 1.57 cm ky^{-1}) with a hiatus between 17.80 to 10.45 cal ka BP (Fig. 14; Supplementary data I, II), coincident with the abrupt colour change mentioned (Fig. 12). Radiocarbon data from core PC01 showed an inverted sequence for the whole core (Fig. 12). The pteropod sample from core PC01 had an age of 19.81 cal ka BP (Supplementary data I).

5. Discussion

5.1. Tectonic control of the surficial sediments on a high marginal platform

5.1.1. Upper tectono-sedimentary architecture

The identification of numerous structural features (fold bulges, anticlines, structural undulations, troughs, pockmarks, giant depression and faults) affecting to the most surficial sediment units (Figs. 4, 5, 6, 7, 8, 9, 10), suggests the importance of the tectonic control over the most recent Late Quaternary sedimentary architecture in the study area (Fig. 15). Tectonic control of the sedimentary record is also reflected and confirmed by the identification of structural deformations in the chirp seismic profiles (Fig. 7b, e, f). These structural deformations are the result of fault deformation that introduce changes in the available accommodation space that combined with the bottom current activity, control the thickness variations observed at the different seismic units described (Figs. 7b, e, f, 15a). Besides, this tectonic deformation, combined with erosional activity, is also the responsible for the truncate reflectors identified in 1C, 1D or 1F echo types (Figs. 2, 7a, b, e, f, 8, 9, 10, 15a). Furthermore, the topographically uplifted surface of the south sector of the TZ morphostructural province resulted in a dome-like morphology (Fig. 3a, c), as well as the presence of numerous structural highs, scarps, giant depressions and troughs governed by faults also indicate a structural control of the complex physiography and the surficial sedimentary architecture of this high marginal platform (Figs. 4, 5, 6). Regarding troughs, these bathymetric lows corresponding to the superficial “cracks” describe by Somola et al., (2019) within the domo-like structure, also characterised as a structural feature confirming their tectonic control (Fig. 15a).

The cause of the intense faulting, folding, and deformation of the upper units (Fig. 15a) identified in this margin is related to the reactivation of the fault Mesozoic system during Cenozoic compression regimes (Vázquez et al., 2008). At the northern Iberian continental margin, the most important Cenozoic compressive deformation occurred during the Eocene related to the Pyrenean orogeny, although this compressive regime has been active until the early Miocene (Burdigalian times) (Pinheiro et al., 1996; Vázquez et al., 2008). These compressive phases had an N-S stress direction, and they were a consequence of the northern convergence of the Iberian Plate and the southward subduction of the Bay of Biscay oceanic crust under the Iberian Margin continental crust (Sibuet et al., 2004). However, from the late Neogene (Tortonian times) to the present day, the rotation of the

Africa-Iberia and Eurasia convergence caused a compressive regime change from N-S to NW-SE trend (Maestro et al., 2018b; Somoza et al., 2019). Thus, the recognition in the scientific literature of neotectonic faults, Quaternary sedimentary instabilities or recent earthquakes activity (Alonso et al., 2008; Díaz et al., 2008; Vázquez et al., 2008; Somoza et al., 2019; Yenes et al., 2019) suggests that these neotectonic NW-SE compressional events also have been present until recent times in the study area.

According to the previous works (Vázquez et al., 2008; 2009b; 2009a; Ercilla et al., 2011; Somoza et al., 2019) the intense deformation and faulting of the post-rift units (Albian to Quaternary) in this margin are related to the presence of a viscous layer corresponds with the “black shale unit” of Albian–Cenomanian age, named as Unit 3 by Murillas et al., (1999) and Ercilla et al., (2008). This layer was the possible responsible agent for the intense plastic and brittle deformation of the upper sediments of the marginal platform (Fig. 15) due to their vertical and horizontal mobility triggered by Cenozoic compression phases (Vázquez et al., 2008). This process also favoured a decoupled between the cover sedimentary and the basement structures and the formation of neotectonic normal faults (Vázquez et al., 2008). The Cenozoic compressional activity mentioned also caused the reactivation of the basement structures, configuring the isolated and elevated marginal platform complex physiography (Vázquez et al., 2008; 2009b; 2009a). Thus, the domo-like morphology, associated to fold bulges located over anticlines structures (Fig. 10), is related to the horst basement reactivation during the Cenozoic, a process that folded the post-rift sediments and uplifted the south sector of the TZ morphostructural province, as demonstrated Vázquez et al., (2008) (Fig. 15b). Attending to the context of the Pyrenean orogeny, the recognition of the N–S to NNE–SSW-oriented fold bulges 1 and 2 (Fig. 4) could be related with the reactivation of Mesozoic N–S fractures that act as normal faults during the N-S compressive regime acting from the Paleogene to the Miocene (Maestro et al., 2018b). On the contrast, the NW–SE-oriented fold bulge 3 (Fig. 4) could be linked with the NW-SE convergence from the late Neogene to present time that reactivated previous NW–SE fractures as normal faults (Maestro et al., 2018b). These successive compression processes could be the responsible for the uplift surface of the south sector of the marginal platform (Fig. 3a, c) and the structural deformation of the recent seismic units described (Figs. 7b, e, f, 15a).

Furthermore, our bathymetric data display NW-SE lineaments, such as faults, troughs, structural undulations or some of the scarps described (Figs. 4, 5, 7, 9) that are parallel to the above mentioned NW-SE compressional regime active from the late Neogene to the present day (Maestro et al., 2018b; Somoza et al., 2019). This fact suggests that the tectonic activity has been active until recent times affecting and controlling the Late Quaternary sedimentary architecture and record of the study area, as well as the bathymetric expression of the current seabed. Therefore, the compressional regimes during the Cenozoic and the plastic behaviour and the mobility of the “black shale unit” layer eased the

development of the different structural and morphological features described in the high marginal platform.

5.1.2. Tectonic control of the giant depressions

Giant depressions have been identified and reported widely around the world (Gay et al., 2006; León et al., 2010; Sun et al., 2011; Chen et al., 2015; 2018; Wenau et al., 2017). In the mentioned scientific literature, the origins of these giant structures are usually attributed to massive fluid escapes in intensely faulted areas associated with diapiric structures at depth formed by plastic material (salt or silt). Moreover, these structures can subsequently be reshaped either by erosive action by sea-bottom currents or by the coalescence of other small pockmarks (e.g., Gay et al., 2006; Sun et al., 2011; García et al., 2016).

The formation of the three giant depressions identified is related to intense deformation and faulting during the Cenozoic compressive regime (Vázquez et al., 2009). These authors suggested that these depressions are related to collapses to the upper sediments related to intense normal faults activity due to diapiric ascends caused by the vertical mobility of the “Black shale unit” described above. This configuration created migration paths through faults for fluid leakage triggering the depression collapses (Fig. 15b) (Vázquez et al., 2009b; Ercilla et al., 2011; Somoza et al., 2019). In our data, the MCS seismic profiles confirm the tectonic control of these structures, where faults are arranged surrounding and inclined toward the centres of the three depressions (Fig. 6). The truncated reflectors over the flanks of the depression also confirm the erosive features of these structures due to the possible large fluids escapes hypothesis (Figs. 6, 9). Furthermore, the NW-SE lineament trend of the three giant depressions in the bathymetric map (Fig. 4) suggests that these features could be associated to the mentioned NW-SE convergence regimes active from the Late Neogene due to fluids venting activity related to diapirs, as also suggest Somoza et al., (2019). The MCS seismic fault analysis developed by Ribeiro, (2011) in the *Gran Burato* area displays principally NNW-SSE orientated faults, confirming that the late Neogene NW-SE compressional deformation triggered the formation of the three giant depressions.

Furthermore, chronological and sedimentological data of cores PC01 and GC16 provide valuable information about the role of recent tectonic activity in the *Gran Burato* depression and their surrounding area. The age-inverted sequence obtained for PC01 core (Fig. 12; Supplementary data I), with ages between 19.81 and 22.17 cal ka BP, could reveal a sedimentary instability of the flanks of the depression due to faults reactivations during the Late Pleistocene. These tectonic pulses would cause the exposure of sediments through the activity of the faults, which facilitated the erosion and removal of seafloor material from depression flanks by vigorous bottom currents and their reposition at the bottom of the *Gran Burato* structure, forming the foraminifera-rich sand facies and the pteropod-rich sand facies (Figs. 1d, 12, 13e, f). Besides, the geochronology obtained for core GC16,

located at the northeast troughs system surrounding *Gran Burato* depression (Fig. 1d), indicates a very low sedimentation rate for the last 30 cal ka BP, with a marked hiatus between 17.80 to 10.45 cal ka BP (Figs. 12, 14: Supplementary data I, II). Although the main remobilisation of the sediments took place by bottom current activity, tectonic pulses occurred during Late Pleistocene could facilitate the remobilisation of recent sediments in the *Gran Burato* surrounding area and their distribution by bottom currents. This assumption indicates that the latest activity of the faults associated with the *Gran Burato* depression and the troughs system took place during the hiatus period mentioned above, confirming the neotectonic control of the giant depressions and troughs. Moreover, the truncated reflectors over the troughs flanks (Figs. 9, 10) suggest that these bathymetric lows act as conduits for the transport of sediments.

These tectonic pulses and their influence on the sedimentary processes were also identified in the neighbouring GB province (Ercilla et al., 2006; Alonso et al., 2008). Those authors described predominant turbidite sedimentation during the Late Pleistocene (from 31.2 to 9.1 ka BP) on the SW flank of the GB associated with tectonic pulses that caused the reactivation of faults scarps and earthquake activity. Moreover, Yenes et al. (2019) estimated and confirmed the role of earthquakes in the remobilisation of sediments in the GB province, demonstrating neotectonic activity in this margin.

5.1.3. Pockmarks feature and current fluid escape activity

The small-scale seafloor depressions recognisable in the chirp and MCS seismic profiles, mostly filled by sediments, are delimited by normal faults, suggesting a structural control (Figs. 8, 9, 10a). These structures with V-morphology, principally located within the 1F echo type, have been interpreted as filled, partially filled and unfilled pockmarks associated with fluid escapes during the Late Quaternary (Fig. 8) (Ribeiro, 2011; Llave et al., 2018). Besides, various authors identified fluid venting features (e.g. transparent columnar facies or acoustic anomalies) in-depth stratigraphic analysis at the surrounding *Gran Burato* depression area (Vázquez et al., 2009b; Ribeiro, 2011; Minshull et al., 2020). This fact supports the hypothesis that these V-morphology depressions could be associated with gravitational collapses formed by migration of fluids. Furthermore, the presence of filled and partially filled pockmarks (Figs. 8, 9, 10) suggests that these structures are currently inactive and undergoing sedimentary deposition. Also, the recognition of pockmarks with various stages of infill suggests that fluid migration to the seafloor could occur in episodic processes dependent on tectonic regime pulses, which evidence nowadays a scarce fluid escape activity.

Additionally, the $\delta^{13}\text{C}$ and $\delta^{18}\text{O}$ isotopic composition values obtained from both GC16 facies indicate marine carbonate isotopic conditions (Joseph et al., 2013). This fact suggests that the cement of the pale high-density facies of core GC16 is not related to methane-derived authigenic carbonates associated with recent methane fluids escapes.

5.2. Sedimentary systems acting at the high marginal platform

5.2.1. (Hemi)pelagic sedimentary system

Pelagic settling of biogenic marine microskeletons and hemipelagic settling of biogenic and terrigenous components by slow lateral advection are the mechanisms responsible for the sedimentation of the pelagite and hemipelagite features identified within the 1B echo type (Fig. 2; Table 2).

Core facies also support this (hemi)pelagic system interpretation. The facies analyses of the PC13-3, PCL1-2 and PC06 cores display a succession of pelagites and hemipelagites layers deposited during the last 172 cal ka BP (Figs. 12, 13a, b, d). Furthermore, some detrital layers appear interbedded into the two previous facies (Figs. 12, 13c). The detrital facies is associated with Heinrich sediments deposited during cold stadials due to the melting of massive icebergs released from ice-sheets, which caused the input of ice-rafted debris (IRD) and melt-water components into the sediments. Similar IRD facies have also been previously described at the Galician Continental Margin (Alonso et al., 2008; Rey et al., 2008; Martins et al., 2013; Plaza-Morlow et al., 2017; Mena et al., 2018). The general low sedimentation rates calculated for the last 172 cal ka BP in all the cores suggests a sediment winnowing of the surficial (hemi)pelagic deposits acting by bottom-current activity (Fig. 14).

5.2.2. Bottom current-controlled (hemi)pelagic sedimentary system

This sedimentary system is originated by the interaction of strong bottom-hugging currents and (hemi)pelagic system, leading to the formation of erosive or non-depositional features. The bottom current-controlled sedimentary system is defined by the 1A, 1C, 1D, 1E and 1F echo types (Fig. 2) that defines erosional surfaces (Table 2).

The non-penetrative 1A echo type is principally located over the slopes that connect at the east and the northwest the TZ morphostructural province to GIB and NF morphostructural provinces, respectively (Fig. 2). This echo could be related to coarse-grained sediments (coarse and silty sands) under erosion at high-energy environments, as suggested by Llave et al., (2018) at the northern Galician Continental Margin. The 1C, 1E and 1F echo types, correspond to erosional surfaces (Table 2) principally located at highest geomorphological areas of the dome-like structure, where fold bulges 1, 2, and 3 are located (Fig. 2). Also, the 1C echo type covers the surrounding area of the top of the east scarps that define the boundary of the TZ morphostructural province, the top of the *Fernando* high, and areas partially surrounding the *Fernando*, *Sancho*, *Barcelona* and *Savoie* highs. Finally, 1D echo type is located mainly over the slopes of the dome-like structure (Fig. 2). These latter four echo types correspond to the mixed features defined by Ercilla et al., (2011), associated with an erosional process acting over the sedimentary cover. Thus, this sedimentary system indicates a topographic control of the bottom current activity throughout the marginal platform, resulting in intense erosion of

the recent sediments in these areas. The main water masses responsible for this sedimentary system are the MOW, LSW and NADW (Fig. 16).

5.2.3. Contourite sedimentary system

This system is responsible for the formation of the different elongated separated drifts and moats that surround the *Barcelona*, *Sancho*, *Savoie* and Galicia Bank structural highs (Figs. 4, 5b, 7a). These highs act as an obstacle for the water masses and induce an acceleration of the bottom current. This phenomenon resulted in the erosion, reshaping and deposition features of the seabed whose geomorphological expression are the moats and drifts identified and characterised by the 1A and 1B echo types, respectively (Fig. 2; Table 2). This system is also responsible for the formation of the sedimentary waves identified at the Galicia Bank plateau by the MOW associated with the 2A echo type (Figs. 2, 4; Table 2). These features are in concordance with the previous contourites system description done by Ercilla et al., (2011) at the Galicia Bank region.

According to the present-day depth of each water masses (Fig. 16), the northwards MOW is responsible for the moats and drifts located until $\sim 1,750$ m of depths (Fig. 4) (e.g., features surrounding the *Barcelona*, *Sancho* and Galicia Bank structural highs); meanwhile the southwards LSW is responsible for the erosional and depositional contourite features identified between $\sim 1,750$ and 2,200 m (Fig. 4) (e.g., moats and drifts surrounding the *Savoie* high and moats associated to the *Málaga* and *Ordoño* highs) (Ercilla et al., 2011). Below $\sim 2,200$ m, the NADW is responsible for the moats identified surrounding the *Fernando* and *A* highs (Figs. 4, 16).

Furthermore, geomorphological features (positive and negative reliefs) and MCS seismic records from the sedimentary fills of the *Orella* and *Crater 3* depressions (Fig. 6), allowed defining a novel type of contourite named as pockmarks-related drift (Fig. 17). This new typology of drift is related to confinement environments, and it shows similarities to other contourites drifts as the confined drifts and channel-related drifts (Stow et al., 2002; Rebesco et al., 2014). In the *Orella* and *Crater 3* depressions, these contourites drifts show mounded elongated drifts separated from the flanks of the depressions by distinct moats (Fig. 17). Their origin is related to the action of the bottom-current over the sediments that fill these structures. When the water mass meets giant depressions, these confined structures produce a constrained of the bottom current, increasing the flow velocity that shaping the seafloor (Stow et al., 2002; Rebesco et al., 2014). As a result, bottom current paths erode the margins of the depression, forming moats (negative reliefs) and separating mounded drifts (positive reliefs) from the flanks (Fig. 17). Besides, the *Orella* depression shows a negative relief over the mound drift related to an axial surficial flow path that erodes the seafloor (Fig. 17).

5.2.4. Downslope sedimentary system

This sedimentary system is characterised by the different erosional and depositional features described caused by downslope processes. At the high marginal platform, these systems act at the different channels systems identified in the geomorphological map and seismic analysis (Figs 4, 7d), as well as at gullies favoured by the presence of scarps (Fig. 4). This system corresponds principally to the 1E, 3A and 3B echo type (Fig. 2; Table 2).

Furthermore, the lower topographic elevation of the TZ north sector facilitates the drainage system of the channels and troughs that flow, respectively from the GB structural high and from the dome-like structure of the TZ south sector to the centre of the north sector, favouring the mass-transport deposits identified in the distal part of this drainage system defined by the 1G echo type (Figs. 2, 4; Table 2).

5.3. Bottom water processes on an isolated high marginal platform

Images from the seafloor have allowed identifying present-day ripples, grooves and comet marks, as well as the presence of ferruginous tubes, pteropods accumulations and dense crusts distributed over the seafloor (Fig. 11), supporting the interpretation of erosional activity by high-intensity bottom current processes. Ferruginous tubes could be related to iron precipitations into the tube-dwelling macrozoobenthos during early diagenesis processes, which were later eroded, remobilised and locally redistributed over the seabed by bottom currents. Similar distribution occurs with the pteropods accumulations. The pteropod layers identified in core PC01 and the pteropod deposits images covering the seafloor (Figs. 11, 12, 13f) could be related to others similar pteropod layers identified from the Senegalese to Iberian coasts (Dieser-Haass and Van der Spoel, 1978; Baas et al., 1997). Regarding the Galician Continental Margin, Alonso et al., (2008) also described pteropod layers associated with debrites on the SW flank of the GB; meanwhile, Mena et al. (2018) also identified rich pteropod layers interbedded in sediments in the vicinity of the GIB province. The ages of these pteropod layers have been mainly dated as between ~ 24 and ~ 18 cal ka BP, coeval with the Last Glacial Maximum. The origin of these pteropods accumulations is still not completely understood. Baas et al., (1997) interpreted the occurrence of these sporadic layers as related to water chemistry changes that induced a decrease in aragonite dissolution because of deepening of the aragonite compensation depth and/or climatic and hydrographic changes related to warmer impulses and decrease in the upwelling system in surface waters (Sarnthein et al., 1982; Alonso et al., 2008). In our study area, radiocarbon dates of rich-pteropod PC01 core display an inverted sequence with an estimated age between 19.8 and 22.2 cal ka BP (Fig. 12; Supplementary data I), coincident within the previously mentioned age of the pteropod-rich layers in the literature. Thus, the pteropod shells identified could have previously been deposited in other areas of the margin during intense mass mortality events, and later were redistributed by deep current activity.

Regarding the dense crusts observed in ROV images (Fig. 11d); these have been associated texturally to the pale high-density silt facies identified in GC16 core (Figs. 12, 13h). These features could be

related to diagenetic processes that caused the dense crusts formation and the slight cementation of the matrix of the high-density silt GC16 facies. The mentioned process took place during the marked temporal hiatus calculated (Fig. 14; Supplementary data I, II), which is coincident with an abrupt change in colouration and density in that core (Fig. 12). This temporal hiatus also demonstrates the presence of a vigorous bottom current influence that erodes sediments, exposing the dense crusts to the seafloor.

Texturally, sediments cores comprise very poorly sorted fine or very fine sands (Table 3 and 4). These mean grain sizes contrast with the fine texture what is expected in deep-sea (hemi)pelagic sediments in isolated ocean areas (Alonso et al., 2008; Mena et al., 2018). These coarser sediments in an offshore source-to-sink sedimentary system, along with the low sedimentation rates obtained in all cores (Fig. 14), suggest a constant erosion of the fine fraction in the high marginal platform. This erosional process is more marked at core PC13-3, PCL1-2, PC01 and GC16 extracted from the most elevated area of the marginal platform, in comparison to PC06 core, which shows the less content in sand and the higher sedimentation rates registered (Figs. 1c, d, 14; Table 3). These data suggest that the erosion capacity is more pronounced at the maximum surface elevation of the domo-like structure that characterises the south sector of the marginal platform, in comparison to the east boundary between the TZ and GIB morphostructural provinces, where is located PC06 core (Fig. 1c).

The large numbers of erosive and control-current features describe, along with the main sedimentary systems acting in this isolate high ocean area that favouring seafloor erosion and sediment winnowing, confirm the influence of vigorous bottom currents acting and reshaping sediments. We proposed that the origins of those bottom-hugging currents are related to both topographic and climatic forcings.

Topographically, the general seafloor elevation of the marginal platform, particularly the domo-like structure of the south sector, and their confinement configuration surrounding by structural highs, especially the GB to the west, cause constriction of the two principal water masses that act in this morphostructural province: the MOW that flows northward and the LSW that flows southward (Figs. 1a, 16). This constriction of the MOW and LSW water masses induces a general intensification of the bottom currents with a velocity increase of the near-bottom water masses. At present-day, this phenomenon increases the erosive capacity of the seafloor currents that affect the most recent sedimentary cover, resulted in the erosional surfaces integrated by 1A, 1C, 1D, 1E and 1F echo types, the low sedimentation rates and the erosion bottom features identified (Figs. 2, 11, 14; Table 2). The erosive action of the bottom currents is greater on the erosional surfaces located in the most topographically elevated areas of the south sector (Fig. 3a, c); this fact also prevents the infill of the Gran Burato depression (Fig. 6). In the case of the erosional surfaces that surround some structural

highs and scarps (Fig. 2; Table 2), their origin could be related to helicoidal flows resulting from the interaction of the bottom current with these topographic features that enhanced their erosion capacity.

Climatically, the low sedimentation rates, especially during cold stadials, and the Heinrich Layer condensed sequences identified (Figs. 12, 14), could be explained by a decrease in palaeoproductivity in stadials in the study area (Voelker et al., 2009; Salgueiro et al., 2010), reflected by lower deposition of marine microskeletons in (hemi)pelagic settling. However, this fact alone does not explain the low sedimentation rates in cold stadials phases (Fig. 14) in contrast with the values obtained close to the study area (Rey et al., 2008; Martins et al., 2013; Mena et al., 2018). Several authors have demonstrated deepening and intensification of the MOW during cold phases in the south sector of the Iberian Continental Margin (Llave et al., 2006; 2015; Voelker et al., 2006), in which the MOW could reach several metres deeper than present conditions (~ 2,000 m). These hydrographic changes and reconfigurations of the water masses could have affected to the sediments of the high marginal platform, as some authors previously suggested in the GB region (Ercilla et al., 2011) and in the southern part of the GIB province (Hanebuth et al., 2015; Zhang et al., 2016; Petrovic et al., 2019). Also, Petrovic et al., (2019) documented a strengthening of the MOW from 17.2 to 9.9 cal ka BP, concordant in age with the hiatus (17.80 to 10.45 cal ka BP) calculated in core GC16 (Figs. 12, 14; Supplementary data I, II). Furthermore, Singh et al., (2015) reported a significant decrease of the MOW strength from 175 to 155 cal ka BP in the Gulf of Cadiz, following by an enhanced of the MOW circulation between 140 and 150 cal ka BP. These findings match with our sedimentation rates obtained within MIS 6 (Fig. 14). The hiatus calculated in core PC13-3 from 155 to 140 cal ka BP is coincident with the MOW intensification reported; meanwhile, the highest sedimentation rates match with the weakened MOW interval. Furthermore, this hiatus is located at ~ 3.40 depth of the core PC13-3, coincident with a grain size change that was correlated with the lower limit of the seismic unit 1 (Fig. 7c). From this depth, the PC13-3 core shows a mostly silt-clay grain size, which suggests a decrease in the erosive activity of the bottom currents (Fig. 7c). Thus, the readjustment of the water masses in cold conditions caused by the weakness of the Atlantic Meridional Overturning Circulation (AMOC) produce the vertical downward migration of a denser and intensified MOW during cold stadials. This phenomenon causes a strengthened of the bottom-hugging currents, already intensified by topographic factors, enhancing the erosion and redistribution of sediments along the high marginal platform, explaining the extremely low sedimentation rates obtained.

6. Conclusions

The integration of a large dataset composed of multibeam bathymetry, chirp and MCS seismic records, and facies analyses carried out based on five piston cores, in conjunction with ROV observations of the seafloor, helped characterise the Late Quaternary tectono-sedimentary features and processes along the isolated and elevated Transitional Zone morphostructural province of the

Galician Continental Margin. The findings obtained from this research point out that the topography of the study area and the hydrographic reorganisations related to climate changes, combined with the tectonic activity, are the main factors that control the Late Quaternary sedimentary dynamic at this isolate and elevated offshore marginal platform.

Topographic and hydrodynamics factors related to climate changes cause a constriction of the water masses and acceleration of bottom flow, favouring seafloor erosion and sediment winnowing, and the redistribution of sediments in the high marginal platform. The vigorous erosional activity produces coarser texturally facies than the typical fine facies of an offshore source-to-sink system. As a novelty, a new typology of contourite has been defined inside the giant depressions: the pockmarks-related drift. Beside, tectonic factors related to Cenozoic compression regime control the accommodation space of the surficial sediments and cause the intense faulting, folding and deformation of the upper sedimentary record, confirming active neotectonic activity until recent times.

Finally, our data provide a new integrated vision of the importance of applying a multiapproach perspective to characterise marine environments to understand with more detail the influence of the tectonic and deep-water circulation changes over the sedimentary dynamic. This multiapproach methodology allowed improving the knowledge about the tectono-sedimentary processes acting at an offshore isolated high marginal platform during the most recent geological past, as is the case of the Galician Continental Margin.

Supplementary data

Supplementary data I. Age models tables for each sedimentary piston core used in this study. The age models have been obtained using ^{14}C dates of the five piston cores used in this research, combined with ^{14}C dates and control-points obtained by the correlation of the five cores with the nearby cores MD95-2040 and MD95-2039, located about ~ 245 kilometres south of the study area (de Abreu et al., 2003; Schönfeld et al., 2003).

Supplementary data II. Age models for the PC13-3, PCL1-2, PC06 and GC16 cores, obtained using the OxCal software v4.3.2.

Available research data

López Pérez, Ángel Enrique (2020), "Sediment data of cores PC13-3, PCL1-2, PC06, PC01 and GC16 (Galician Continental Margin)", Mendeley Data, V1, doi: 10.17632/bpj2tvjynh.1

Seismic data is available on request.

Acknowledgements

This work was funded by the Gran Burato 2010 and 2011 agreement between the University of Vigo, CSIC, and Xunta de Galicia, and by MINECO Project CGL2008-034774-E. We thank the captains and crew of the R/V *Sarmiento de Gamboa*, the UTM technical support, and the GB4240 and GB2011 cruise participants and Soledad García Gil for sharing the chirp seismic data acquired during ERGAP C cruise. A.E. López Pérez was awarded a PhD fellowship by the Xunta de Galicia (Department of Culture, Education and University Planning) supported by the European Social Fund 2014/2020. M. Plaza-Morlote was awarded a Postdoctoral fellowship by the Xunta de Galicia (Department of Culture, Education and University Planning) supported by the European Social Fund 2014/2020.

References

- Abreu, L. de, Shackleton, N.J., Schönfeld, J., Hall, M., Chapman, M., 2003. Millennial-scale oceanic climate variability off the Western Iberian margin during the last two glacial periods. *Marine Geology* 196, 1–20. doi:10.1016/S0025-3227(03)00455-X
- Alonso, B., Ercilla, G., Casas, D., Estrada, F., Farrán, M., García, M., Rey, D., Rubio, B., 2008. Late Pleistocene and Holocene sedimentary facies on the SW Galicia Bank (Atlantic NW Iberian Peninsula). *Marine Geology* 249, 46–63. doi:10.1016/j.margeo.2007.09.012
- Baas, J.H., Mienert, J., Abrantes, F., Prins, M.A., 1997. Late Quaternary sedimentation on the Portuguese continental margin: climate-related processes and products. *Palaeogeography, Palaeoclimatology, Palaeoecology* 130, 1–23. doi:10.1016/S0031-0182(96)00135-6
- Bender, V.B., Hanebuth, T.J.J., Mena, A., Baumann, K.-H., Francés, G., Dobeneck, T. von, 2012. Control of sediment supply, palaeogeography and morphology on late Quaternary sediment dynamics at the Galician continental slope. *Geo-Marine Letters* 32, 313–335. doi:10.1007/s00367-012-0282-2
- Bezerra, F.H., Castro, D.L. de, Maia, R.P., Sousa, M.O.L., Moura-Lima, E.N., Rossetti, D.F., Bertotti, G., Souza, Z.S., Nogueira, F.C.C., 2020. Postrift stress field inversion in the Potiguar Basin, Brazil – Implications for petroleum systems and evolution of the equatorial margin of South America. *Marine and Petroleum Geology* 111, 88–104. doi:10.1016/j.marpetgeo.2019.08.001
- Bezerra, F.H.R., Brito Neves, B.B., Corrêa, A.C.B., Barreto, A.M.F., Suguio, K., 2008. Late Pleistocene tectonic-geomorphological development within a passive margin — The Cariatá trough, northeastern Brazil. *Geomorphology* 97, 555–582. doi:10.1016/j.geomorph.2007.09.008
- Boillot, G., Malod, J., 1988. The north and north-west Spanish continental margin: a review. *Rev Soc Geol España* 1, 295–316.
- Boillot, G., Dupeuble, P.A., Malod, J., 1979. Subduction and tectonics on the continental margin off northern Spain. *Marine Geology* 32, 53–70. doi:10.1016/0025-3227(79)90146-4
- Boillot, G., Grimaud, S., Mauffret, A., Mougénot, D., Kornprobst, J., Mergoïl-Daniel, J., Torrent, G., 1980. Ocean-continent boundary off the Iberian margin: A serpentinite diapir west of the Galicia Bank. *Earth and Planetary Science Letters* 48, 23–34. doi:10.1016/0012-821X(80)90166-1
- Chen, J., Song, H., Guan, Y., Yang, S., Pinheiro, L.M., Bai, Y., Liu, B., Geng, M., 2015. Morphologies, classification and genesis of pockmarks, mud volcanoes and associated fluid escape features in the northern Zhongjiannan Basin, South China Sea. *Deep Sea Research Part II: Topical Studies in Oceanography* 122, 106–117. doi:10.1016/j.dsr2.2015.11.007

- Chen, J., Song, H., Guan, Y., Pinheiro, L.M., Geng, M., 2018. Geological and oceanographic controls on seabed fluid escape structures in the northern Zhongjiannan Basin, South China Sea. *Journal of Asian Earth Sciences* 168, 38–47. doi:10.1016/j.jseaes.2018.04.027
- Damuth, J.E., 1980. Use of high-frequency (3.5–12 kHz) echograms in the study of near-bottom sedimentation processes in the deep-sea: A review. *Marine Geology* 38, 51–75. doi:10.1016/0025-3227(80)90051-1
- Dean, S.L., Sawyer, D.S., Morgan, J.K., 2015. Galicia Bank ocean–continent transition zone: New seismic reflection constraints. *Earth and Planetary Science Letters* 413, 197–207. doi:10.1016/j.epsl.2014.12.045
- Díaz, J., Gallart, J., Gaspà, O., Ruiz, M., Córdoba, D., 2008. Seismicity analysis at the Prestige oil-tanker wreck area (Galicia Margin, NW of Iberia). *Marine Geology* 249, 150–165. doi:10.1016/j.margeo.2007.09.015
- Diester-Haass, L., Van der Spoel, S., 1978. Late Pleistocene pteropod-rich sediment layer in the Northeast Atlantic and protoconch variation of *Clio pyramidata* Linné 1767. *Palaeogeography, Palaeoclimatology, Palaeoecology* 24, 85–109. doi:https://doi.org/10.1016/0031-0182(78)90001-9
- Druet, M., 2015. Geodinámica del Margen Continental de Galicia: Estructura Profunda y Morfotectónica. PhD thesis. Madrid Complutense University.
- Ercilla, G., Córdoba, D., Gallart, J., Gràcia, E., Muñoz, J.A., Somoza, L., Vázquez, J.T., Vilas, F., 2006. Geological characterization of the Prestige sinking area. *Marine Pollution Bulletin* 53, 208–219. doi:10.1016/j.marpolbul.2006.03.016
- Ercilla, G., García-Gil, S., Estrada, F., Gràcia, E., Vizcaino, A., Vázquez, J.T., Díaz, S., Vilas, F., Casas, D., Alonso, B., Dañobeitia, J., Farran, M., 2008. High resolution seismic stratigraphy of the Galicia Bank Region and neighbouring abyssal plains (NW Iberian continental margin). *Marine Geology* 249, 108–127. doi:10.1016/j.margeo.2007.09.009
- Ercilla, G., Casas, D., Vázquez, J.T., Iglesias, J., Somoza, L., Juan, C., Medialdea, T., León, R., Estrada, F., García-Gil, S., Farran, M., Bojórquez, F., García, M., Maestro, A., 2011. Imaging the recent sediment dynamics of the Galicia Bank region (Atlantic, NW Iberian Peninsula). *Marine Geophysical Research* 29, 119–126. doi:10.1007/s11001-011-9129-x
- Fiúza, A.F.G., Hamann, M., Ambar, I., Díaz del Río, G., González, N., Cabanas, J.M., 1998. Water masses and their circulation off western Iberia during May 1993. *Deep Sea Research Part I: Oceanographic Research Papers* 45, 1127–1160. doi:10.1016/S0967-0637(98)00008-9
- García, M., Hernández-Molina, F.J., Alonso, B., Vázquez, J.T., Ercilla, G., Llave, E., Casas, D., 2016. Erosive sub-circular depressions on the Guadalquivir Bank (Gulf of Cadiz): Interaction between bottom current, mass-wasting and tectonic processes. *Marine Geology* 378, 5–19. doi:10.1016/j.margeo.2015.10.004
- Gay, A., Lopez, M., Ondreas, H., Charlou, J.-L., Sermondadaz, G., Cochonat, P., 2006. Seafloor facies related to upward methane flux within a Giant Pockmark of the Lower Congo Basin. *Marine Geology* 226, 81–95. doi:10.1016/j.margeo.2005.09.011
- Group Galice, 1979. The continental margin off Galicia and Portugal: acoustical stratigraphy, dredge stratigraphy and structural evolution. In: Sibuet, J.C., Ryan, W.B.F. et al. (Eds.), *Init. Repts. D.S.D.P.*, 47 (2), U.S. Govt. Printing Office, Washington, p., 622–633. doi:10.2973/dsdp.proc.47-2.1979
- Hall, I.R., McCave, I.N., 2000. Palaeocurrent reconstruction, sediment and thorium focussing on the Iberian margin over the last 140 ka. *Earth and Planetary Science Letters* 178, 151–164. doi:10.1016/S0012-821X(00)00068-6
- Hanebuth, T.J.J., Zhang, W., Hofmann, A.L., Löwemark, L.A., Schwenk, T., 2015. Oceanic density fronts steering bottom-current induced sedimentation deduced from a 50 ka contourite-drift record and numerical modeling (off NW Spain). *Quaternary Science Reviews* 112, 207–225. doi:10.1016/j.quascirev.2015.01.027

- Heinrich, H., 1988. Origin and Consequences of Cyclic Ice Rafting in the Northeast Atlantic Ocean During the Past 130,000 Years. *Quaternary Research* 29, 142–152. doi:10.1016/0033-5894(88)90057-9
- Hernández-Molina, F.J., Serra, N., Stow, D.A.V., Llave, E., Ercilla, G., Van Rooij, D., 2011. Along-slope oceanographic processes and sedimentary products around the Iberian margin. *Geo-Marine Letters* 31, 315–341. doi:10.1007/s00367-011-0242-2
- Jané, G., Maestro, A., Ercilla, G., López-Martínez, J., De Andrés, J.R., Casas, D., González-Aller, D., Catalán-Morollón, M., 2010. Occurrence of pockmarks on the Ortegá Spur continental margin, Northwestern Iberian Peninsula. *Marine and Petroleum Geology* 27, 1551–1564. doi:10.1016/j.marpetgeo.2010.04.001
- Joseph, C., Campbell, K.A., Torres, M.E., Martin, R.A., Pohlman, J.W., Riedel, M., Rose, K., 2013. Methane-derived authigenic carbonates from modern and paleoseeps on the Cascadia margin: Mechanisms of formation and diagenetic signals. *Palaeogeography, Palaeoclimatology, Palaeoecology* 390, 52–67. doi:10.1016/j.palaeo.2013.01.012
- León, R., Somoza, L., Medialdea, T., Hernández-Molina, F.J., Vázquez, J.T., Díaz-del-Río, V., González, F.J., 2010. Pockmarks, collapses and blind valleys in the Gulf of Cádiz. *Geo-Marine Letters* 30, 231–247. doi:10.1007/s00367-009-0169-z
- Llave, E., Schönfeld, J., Hernández-Molina, F.J., Mulder, T., Somoza, L., Díaz del Río, V., Sánchez-Almazo, I., 2006. High-resolution stratigraphy of the Mediterranean outflow contourite system in the Gulf of Cadiz during the late Pleistocene: The impact of Heinrich events. *Marine Geology* 227, 241–262. doi:10.1016/j.margeo.2005.11.015
- Llave, E., García, M., Pérez, C., Sayago, M., Farrán, M., Ercilla, G., Somoza, L., León, R., Maestro, A., Medialdea, T., Hernández-Molina, F.J., Álvarez, F., Durán, R., Mohamed, K., 2008. Morphological feature analyses of the Prestige half-graben on the SW Galicia Bank. *Marine Geology* 249, 7–20. doi:10.1016/j.margeo.2007.09.010
- Llave, E., Hernández-Molina, F.J., Ercilla, G., Roque, C., Rooij, D.V., García, M., Juan, C., Mena, A., Brackenridge, R., Jané, G., Stow, D., Gómez-Ballesteros, M., 2015. Bottom current processes along the Iberian continental margin. *Boletín Geológico y Minero* 126 (2–3), 219–256.
- Llave, E., Jané, G., Maestro, A., López-Martínez, J., Hernández-Molina, F.J., Mink, S., 2018. Geomorphological and sedimentary processes of the glacially influenced northwestern Iberian continental margin and abyssal plains. *Geomorphology* 312, 60–85. doi:10.1016/j.geomorph.2018.03.022
- Llave, E., Hernández-Molina, F.J., García, M., Ercilla, G., Roque, C., Juan, C., Mena, A., Preu, B., Van Rooij, D., Rebesco, M., Brackenridge, R., Jané, G., Gómez-Ballesteros, M., Stow, D., 2019. Contourites along the Iberian continental margins: conceptual and economic implications. *Geological Society, London, Special Publications* 476, 403–436. doi:10.1144/SP476-2017-46
- López Pérez, A.E., Rey, D., Martins, V., Plaza-Morlote, M., Rubio, B., 2019. Application of multivariate statistical analyses to Itrax core scanner data for the identification of deep-marine sedimentary facies: A case study in the Galician Continental Margin. *Quaternary International* 514, 152–160. doi:10.1016/j.quaint.2018.06.035
- Maestro, A., López-Martínez, J., Llave, E., Bohoyo, F., Acosta, J., Hernández-Molina, F.J., Muñoz, A., Jané, G., 2013. Geomorphology of the Iberian Continental Margin. *Geomorphology* 196, 13–35. doi:10.1016/j.geomorph.2012.08.022
- Maestro, A., Jané, G., Fernández-Saéz, F., Llave, E., Bohoyo, F., Navas, J., Mink, S., Gómez-Ballesteros, M., Martín-Dávila, J., Catalán, M., 2018a. Echo-character of the NW Iberian continental margin and the adjacent abyssal plains. *Journal of Maps* 14, 56–67. doi:10.1080/17445647.2018.1424653
- Maestro, A., Jané, G., Llave, E., López-Martínez, J., Bohoyo, F., Druet, M., 2018b. The role of tectonic inheritance in the morphostructural evolution of the Galicia continental margin and adjacent abyssal plains from digital bathymetric model (DBM) analysis (NW Spain). *International Journal of Earth Sciences* 107, 1267–1286. doi:10.1007/s00531-017-1531-4

- Martins, V.A., Santos, J.F., Mackensen, A., Dias, J.A., Ribeiro, S., Moreno, J.C., Soares, A.M., Frontalini, F., Rey, D., Rocha, F., 2013. The sources of the glacial IRD in the NW Iberian Continental Margin over the last 40 ka. *Quaternary International* 318, 128–138. doi:10.1016/j.quaint.2013.08.026
- McCave, I.N., Hall, I.R., 2002. Turbidity of waters over the Northwest Iberian continental margin. *Progress in Oceanography* 52, 299–313. doi:10.1016/S0079-6611(02)00012-5
- Medialdea, T., Somoza, L., León, R., Farrán, M., Ercilla, G., Maestro, A., Casas, D., Llave, E., Hernández-Molina, F.J., Fernández-Puga, M.C., Alonso, B., 2008. Multibeam backscatter as a tool for sea-floor characterization and identification of oil spills in the Galicia Bank. *Marine Geology* 249, 93–107. doi:10.1016/j.margeo.2007.09.007
- Mena, A., Francés, G., Pérez-Arлуca, M., Aguiar, P., Barreiro-Vázquez, J.D., Iglesias, A., Barreiro-Lois, A., 2015. A novel sedimentological method based on CT-scanning: Use for tomographic characterization of the Galicia Interior Basin. *Sedimentary Geology* 321, 123–138. doi:10.1016/j.sedgeo.2015.03.007
- Mena, A., Francés, G., Pérez-Arлуca, M., Hanebuth, T.J.J., Bender, V.B., Nombela, M.A., 2018. Evolution of the Galicia Interior Basin over the last 60 ka: sedimentary processes and palaeoceanographic implications. *Journal of Quaternary Science* 33, 536–549. doi:10.1002/jqs.3032
- Minshull, T.A., Marín-Moreno, H., Betlem, P., Bialas, J., Bünz, S., Burwicz, E., Cameselle, A.L., Cifci, G., Giustiniani, M., Hillman, J.I.T., Hölz, S., Hopper, J.F., Iñan, G., León, R., Magalhaes, V., Makovsky, Y., Mata, M.-P., Max, M.D., Nielsen, T., Okay, S., Ostrovsky, I., O'Neill, N., Pinheiro, L.M., Plaza-Faverola, A.A., Rey, D., Roy, S., Schwalenberg, K., Senger, K., Vadakkepuliambatta, S., Vasilev, A., Vázquez, J. T., 2020. Hydrate occurrence in Europe: A review of available evidence. *Marine and Petroleum Geology* 111, 735–764. doi:10.1016/j.marpetgeo.2019.08.014
- Montadert, L., Winnock, E., Deltiel, J.R., Grau, G., 1974. Continental Margins of Galicia-Portugal and Bay of Biscay. In: Burk, C.A., Drake, C.L. (Eds.), *The Geology of Continental Margins*. Springer Berlin Heidelberg, Berlin, Heidelberg, pp. 323–342. doi:10.1007/978-3-662-01141-6_24
- Murillas, J., Mougnot, D., Boulot, G., Cornu, M.C., Banda, E., Mauffret, A., 1990. Structure and evolution of the Galicia Interior Basin (Atlantic western Iberian continental margin). *Tectonophysics* 184, 297–329. doi:10.1016/0040-1951(90)90445-E
- Pellegrini, C., Maselli, V., Trincardi, F., 2016. Pliocene–Quaternary contourite depositional system along the south-western Adriatic margin: changes in sedimentary stacking pattern and associated bottom currents. *Geo-Marine Letters* 36, 67–79. doi:10.1007/s00367-015-0424-4
- Pérez-Gussinyé, M., Ranero, C.J., Reston, T.J., Sawyer, D., 2003. Mechanisms of extension at nonvolcanic margins: Evidence from the Galicia interior basin, west of Iberia. *Journal of Geophysical Research: Solid Earth* 108(B5), 2245. doi:10.1029/2001JB000901
- Petrovic, A., Lantzsch, H., Schwenk, T., Marquardt, J., Titschack, J., Hanebuth, T.J.J., 2019. Post-LGM upward shift of the Mediterranean Outflow Water recorded in a contourite drift off NW Spain. *Marine Geology* 407, 334–349. doi:10.1016/j.margeo.2018.11.015
- Pinheiro, L.M., Wilson, R.C.L., Pena dos Reis, R., Whitmarsh, R.B., Ribeiro, A., 1996. The western Iberia margin: a geophysical and geological overview, In: Whitmarsh, R.B., Daywer, D., Klaus, A., Masson, D.G. (Eds.), *Proc. ODP, Leg 149, Scientific Results Volume 149*, pp. 3–23. doi:10.2973/odp.proc.sr.149.1996
- Plaza-Morlote, M., Rey, D., Santos, J.F., Ribeiro, S., Heslop, D., Bernabeu, A., Mohamed, K.J., Rubio, B., Martins, V., 2017. Southernmost evidence of large European Ice Sheet-derived freshwater discharges during the Heinrich Stadials of the Last Glacial Period (Galician Interior Basin, Northwest Iberian Continental Margin). *Earth and Planetary Science Letters* 457, 213–226. doi:10.1016/j.epsl.2016.10.020
- Pratson, L.F., Laine, E.P., 1989. The relative importance of gravity-induced versus current-controlled sedimentation during the Quaternary along the Mideast U.S. outer continental margin

- revealed by 3.5 kHz echo character. *Marine Geology* 89, 87–126. doi:10.1016/0025-3227(89)90029-7
- Ramsey, C.B., 2008. Deposition models for chronological records. *Quaternary Science Reviews* 27, 42–60. doi:10.1016/j.quascirev.2007.01.019
- Ramsey, C.B., 2017. Methods for Summarizing Radiocarbon Datasets. *Radiocarbon* 59, 1809–1833. doi:10.1017/RDC.2017.108
- Ranero, C.R., Pérez-Gussinyé, M., 2010. Sequential faulting explains the asymmetry and extension discrepancy of conjugate margins. *Nature* 468, 294–299. doi:10.1038/nature09520
- Rebesco, M., Hernández-Molina, F.J., Van Rooij, D., Wåhlin, A., 2014. Contourites and associated sediments controlled by deep-water circulation processes: State-of-the-art and future considerations. *Marine Geology* 352, 111–154. doi:10.1016/j.margeo.2014.03.011
- Reimer, P.J., Bard, E., Bayliss, A., Beck, J.W., Blackwell, P.G., Ramsey, C.B., Buck, C.E., Cheng, H., Edwards, R.L., Friedrich, M., Grootes, P.M., Guilderson, T.P., Hafliðason, H., Hajdas, I., Hatté, C., Heaton, T.J., Hoffmann, D.L., Hogg, A.G., Hughen, K.A., Kaiser, K.F., Kromer, B., Manning, S.W., Niu, M., Reimer, R.W., Richards, D.A., Scott, E.M., Soutter, J.R., Staff, R.A., Turney, C.S.M., Plicht, J. van der, 2013. IntCal13 and Marine13 Radiocarbon Age Calibration Curves 0–50,000 Years cal BP. *Radiocarbon* 55, 1869–1887. doi:10.1017/azul.js.rc.55.16947
- Reston, T.J., 2005. Polyphase faulting during the development of the west Galicia rifted margin. *Earth and Planetary Science Letters* 237, 561–576. doi:10.1016/j.epsl.2005.06.019
- Rey, D., Rubio, B., Mohamed, K., Vilas, F., Alonso, B., Ercilla, C., Kivas, T., 2008. Detrital and early diagenetic processes in Late Pleistocene and Holocene sediments from the SW Galicia Bank inferred from high-resolution enviromagnetic and geochemical records. *Marine Geology* 249, 64–92. doi:10.1016/j.margeo.2007.09.013
- Ribeiro, T., 2011. Multichannel Seismic Investigation of the Gran Burato Area, off W Galicia. MSc thesis. University of Aveiro.
- Rodríguez-Germade, I., Rubio, B., Rey, D., Vilas, F., Martins, V., Rocha, F., 2013. Evaluation of data processing techniques for marine sediments analyzed with an Itrax Core Scanner. *Geogaceta* 53, 85–87.
- Salgueiro, E., Voelker, A.H.L., Abreu, L. de, Abrantes, F., Meggers, H., Wefer, G., 2010. Temperature and productivity changes off the western Iberian margin during the last 150 ky. *Quaternary Science Reviews* 29, 680–695. doi:10.1016/j.quascirev.2009.11.013
- Salgueiro, E., Naughton, F., Voelker, A.H.L., Abreu, L. de, Alberto, A., Rossignol, L., Duprat, J., Magalhães, V.H., Vaquero, S., Turon, J.-L., Abrantes, F., 2014. Past circulation along the western Iberian margin: a time slice vision from the Last Glacial to the Holocene. *Quaternary Science Reviews* 106, 316–329. doi:10.1016/j.quascirev.2014.09.001
- Sarnthein, M., Thiede, J., Flaumann, U., Erlenkeuser, H., Fütterer, D., Koopmann, B., Lange, H., Seibold, E., 1982. Atmospheric and Oceanic Circulation Patterns off Northwest Africa During the Past 25 Million Years. In: Rad, U. von, Hinz, K., Sarnthein, M., Seibold, E. (Eds.), *Geology of the Northwest African Continental Margin*. Springer Berlin Heidelberg, Berlin, Heidelberg, pp. 545–604. doi:10.1007/978-3-642-68409-8_24
- Schönfeld, J., Zahn, R., Abreu, L. de, 2003. Surface and deep water response to rapid climate changes at the Western Iberian Margin. *Global and Planetary Change* 36, 237–264. doi:10.1016/S0921-8181(02)00197-2
- Séranne, M., Abeigne, C.-R.N., 1999. Oligocene to Holocene sediment drifts and bottom currents on the slope of Gabon continental margin (west Africa) Consequences for sedimentation and southeast Atlantic upwelling. *Sedimentary Geology* 128, 179–199. doi:https://doi.org/10.1016/S0037-0738(99)00069-X
- Séranne, M., Anka, Z., 2005. South Atlantic continental margins of Africa: A comparison of the tectonic vs climate interplay on the evolution of equatorial west Africa and SW Africa margins. *Journal of African Earth Sciences* 43, 283–300. doi:10.1016/j.jafrearsci.2005.07.010

- Sibuet, J.-C., Srivastava, S.P., Spakman, W., 2004. Pyrenean orogeny and plate kinematics. *Journal of Geophysical Research: Solid Earth* 109, B08104. doi:10.1029/2003JB002514
- Singh, A.D., Rai, A.K., Tiwari, M., Naidu, P.D., Verma, K., Chaturvedi, M., Niyogi, A., Pandey, D., 2015. Fluctuations of Mediterranean Outflow Water circulation in the Gulf of Cadiz during MIS 5 to 7: Evidence from benthic foraminiferal assemblage and stable isotope records. *Global and Planetary Change* 133, 125–140. doi:10.1016/j.gloplacha.2015.08.005
- Somoza, L., Medialdea, T., González, F.J., León, R., Palomino, D., Rengel, J., Fernández-Salas, L.M., Vázquez, J.T., 2019. Morphostructure of the Galicia continental margin and adjacent deep ocean floor: From hyperextended rifted to convergent margin styles. *Marine Geology* 407, 299–315. doi:10.1016/j.margeo.2018.11.011
- Stow, D.A.V., Faugères, J.-C., Howe, J.A., Pudsey, C.J., Viana, A.R., 2002. Bottom currents, contourites and deep-sea sediment drifts: current state-of-the-art. *Geological Society, London, Memoirs* 22, 7–20. doi:10.1144/GSL.MEM.2002.022.01.02
- Stríkis, N.M., Cruz, F.W., Barreto, E.A.S., Naughton, F., Vuille, M., Cheng, H., Voelker, A.H.L., Zhang, H., Karmann, I., Edwards, R.L., Auler, A.S., Santos, R.V., Sales, P.R., 2018. South American monsoon response to iceberg discharge in the North Atlantic. *Proceedings of the National Academy of Sciences* 115, 3788–3793. doi:10.1073/pnas.1712784115
- Sun, Q., Wu, S., Hovland, M., Luo, P., Lu, Y., Qu, T., 2011. The morphologies and genesis of megapockmarks near the Xisha Uplift, South China Sea. *Marine and Petroleum Geology* 28, 1146–1156. doi:10.1016/j.marpetgeo.2011.03.003
- Thommeret, M., Boillot, G. (Eds.), 1988. Structural map of the Galician margin, In: Boillot, G., Winterer, E.L., et al. (Eds.), *Proc. ODP. Sci. Results vol. 103*, 31–36. *Ocean Drilling Program*. doi:10.2973/odp.proc.sr.103.1988
- Thomson, J., Nixon, S., Summerhayes, C.P., Schönfeld, J., Zahn, R., Grootes, P., 1999. Implications for sedimentation changes on the Iberian margin over the last two glacial/interglacial transitions from (230 Th excess) $\delta^{18}O$ systematics. *Earth and Planetary Science Letters* 165, 255–270. doi:https://doi.org/10.1016/S0012-821X(98)00265-9
- Tucholke, B.E., Sawyer, D.S., Sibuet, J.-C., 2007. Breakup of the Newfoundland–Iberia rift. *Geological Society, London, Special Publications* 282, 9–46. doi:10.1144/SP282.2
- Vanney, J.R., F. Auxièrre, J.L., Dunand, F., 1979. Geomorphic provinces and the evolution of the NorthWestern Iberian Continental Margin. *Ann. Inst. Oceanogr. Paris* 55 (1), 5–20.
- Varela, R.A., Rosón, G., Herrera, J., Torres-López, S., Fernández-Romero, A., 2005. A general view of the hydrographic and dynamical patterns of the Rías Baixas adjacent sea area. *Journal of Marine Systems* 54, 97–113. doi:10.1016/j.jmarsys.2004.07.006
- Vázquez, J.T., Medialdea, T., Ercilla, G., Somoza, L., Estrada, F., Fernández Puga, M.C., Gallart, J., Gràcia, E., Maestri, A., Sayago, M., 2008. Cenozoic deformational structures on the Galicia Bank Region (NW Iberian continental margin). *Marine Geology* 249, 128–149. doi:10.1016/j.margeo.2007.09.014
- Vázquez, J.T., Ercilla, G., Medialdea, T., Somoza, L., Bohoyo, F., Estrada, F., León, R., 2009a. Deformaciones neotectónicas en la Zona Transicional de la región del Banco de Galicia. In: 6th Symposium on the Iberian Atlantic Margin MIA09, Oviedo, pp. 45–48. doi:10.13140/2.1.4571.8723
- Vázquez, J.T., Ercilla, G., Medialdea, T., Somoza, L., Bohoyo, F., Casas, D., Estrada, F., Farrán, M., García-Gil, S., León, R., 2009b. El colapso BURATO ERGAP: Un rasgo morfo-tectónico de primera magnitud en el Banco de Galicia. In: 6th Symposium on the Iberian Atlantic Margin MIA09, Oviedo, pp. 205–208. doi:10.13140/2.1.5161.6963
- Verdicchio, G., Trincardi, F., Asioli, A., 2007. Mediterranean bottom-current deposits: an example from the Southwestern Adriatic Margin. *Geological Society, London, Special Publications* 276, 199–224. doi:10.1144/GSL.SP.2007.276.01.10
- Voelker, A.H.L., Abreu, L. de, 2011. A Review of Abrupt Climate Change Events in the Northeastern Atlantic Ocean (Iberian Margin): Latitudinal, Longitudinal, and Vertical Gradients. In: Rashid,

- H., Polyak, L., Mosley-Thompson, E. (Eds.), Geophysical Monograph Series. American Geophysical Union, Washington, D. C., pp. 15–37. doi:10.1029/2010GM001021
- Voelker, A.H.L., Lebreiro, S., Schonfeld, J., Cacho, I., Erlenkeuser, H., Abrantes, F., 2006. Mediterranean outflow strengthening during northern hemisphere coolings: A salt source for the glacial Atlantic? *Earth and Planetary Science Letters* 245, 39–55. doi:10.1016/j.epsl.2006.03.014
- Voelker, A.H.L., Abreu, L. de, Schönfeld, J., Erlenkeuser, H., Abrantes, F., 2009. Hydrographic conditions along the western Iberian margin during marine isotope stage 2. *Geochemistry, Geophysics, Geosystems* 10, Q12U08. doi:10.1029/2009GC002605
- Wenau, S., Spieß, V., Pape, T., Fekete, N., 2017. Controlling mechanisms of giant deep water pockmarks in the Lower Congo Basin. *Marine and Petroleum Geology* 83, 140–157. doi:10.1016/j.marpetgeo.2017.02.030
- Yenes, M., Casas, D., Nespereira, J., Monterrubio, S., Ercilla, G., López-González, N., 2019. Galicia Bank sediment transport activity in response to continuous sedimentary instability dynamics: a geotechnical perspective. *International Journal of Earth Sciences* 108, 2545–2560. doi:10.1007/s00531-019-01776-w
- Zhang, W., Hanebuth, T.J.J., Stöber, U., 2016. Short-term sediment dynamics on a meso-scale contourite drift (off NW Iberia): Impacts of multi-scale oceanographic processes deduced from the analysis of mooring data and numerical modelling. *Marine Geology* 378, 81–100. doi:10.1016/j.margeo.2015.12.006

Figure captions

Fig. 1. a) Bathymetric map of the Galician Continental Margin (NW Iberian Margin), illustrating the locations of the six main morphostructural provinces defined by Vázquez et al., (2008): the Galicia Interior Basin (GIB), Transitional Zone (TZ), Galicia Bank (GB), Northwestern Flank (NF), Deep Galicia Margin (DGM), and Half-Graben Domain (HGD). Location map also includes a schematic representation of the current superficial, intermediate and deep water masses circulation around the West Iberian Continental Margin (modified from Hernández-Molina et al., 2011; Llave et al., 2019). The water masses are; ENACW_{sp} = Eastern North Atlantic Central Water (subpolar); ENACW_{st} = Eastern North Atlantic Central Water (subtropical); MOW= Mediterranean Outflow Water; LSW= Labrador Sea Water; NADW= North Atlantic Deep Water; LDW= Lower Deep Water; b) location map of the TZ morphostructural province with the transects of the chirp seismic dataset obtained in the MARBANGA and ERGAP C cruises; c) detail map of the south sector of the TZ morphostructural province with the multi-channel and chirp seismic grid acquired during the *Burato 4240* cruise and the positions of piston cores; d) detail map of the *Gran Burato* area with the chirp seismic grid acquired during the MARBANGA cruise and the locations of piston cores. Black lines labelled with capital letters in b), c), and d) refer to the locations of the seismic lines illustrated in Figs. 6, 7, 8, 9, 10;

meanwhile, red dash lines refer to the seismic lines corresponding of each echo type include in Table 2.

Fig. 2. Hillshade map of the TZ morphostructural province with the classification and distribution of the ten high-frequency echo type characters identified in the study area: distinct echoes (1A, 1B, 1C, 1D, 1E, 1F, and 1G), wavy echoes (2A), and hyperbolic echoes (3A and 3B). For more detail of the different echo types, see Table 2. Main geomorphological features are illustrated superimposed over the distribution of the echo type characters.

Fig. 3. a) Bathymetric map of the NW–SE-elongated and elevated marginal platform, named as TZ morphostructural province, obtained from the multibeam echosounder data acquired during the *MARBANGA*, *Gran Burato 4240* and *GALINCLIMARCH* cruises, combined with the bathymetric survey data from the EMODnet Digital Terrain Model repository (emodnet-bathymetry.eu). The red dashed line separates the north and south geomorphological sectors. Note that the south sector shows three maximum surface elevations, configuring a general elevation of this area in comparison with the north sector; b) slope map of the TZ morphostructural province with the location of the giant depressions and structural highs. The highest slopes correspond mainly to scarps and structural highs; c) south and north sectors topographic profiles at $42^{\circ} 40' N$ and $43^{\circ} 0' N$, respectively. The south sector profile shows the dome-like structure that characterises geomorphologically this sector, coincident with the maximum surface elevations identified in the bathymetric map. The north sector profile shows a flat surface. The black dashed lines in 3a and b indicate the location of the bathymetric profiles.

Fig. 4. Hillshade map of the study area illustrating the main morphological features identified along the TZ morphostructural province. Green polygon delimits the limits of this morphostructural province. The white lines indicate the position of the bathymetric lines represented in Fig. 5a-g.

Fig. 5. A set of bathymetric profiles showing the geomorphological features described; a) bathymetric lows caused by faults; b) scarps, moats and drifts; c) fold bulges; d) structural undulations; e) gullies; f) troughs; and g) channels. See the location of the bathymetric profiles in Fig. 4 (P5.a-g); h)

Southeast three-dimensional perspective of the Transitional Zone morphostructural province, illustrating the main geomorphological features described (e.g. structural highs, giant depressions, fold bulges, structural undulations, channels and troughs). The representation shows the general elevation of the south sector that configures the domo-like structure, in comparison with the flat north sector.

Fig. 6. Bathymetric maps and S–N and W–E multi-channel seismic profiles with a ~5X vertical exaggeration (VE) of the three giant depressions identified in the south sector of the TZ morphostructural province: *Gran Burato*, *Crater 3* and *A Orella* depressions. The *Gran Burato* depression is unfilled of sediments, in contrast to *Crater 3* and *A Orella* depressions. In these latter two depressions, it is possible to identify different seismic units filling the depressions, named as C1 and C2 in *Crater 3* depression and O1, O2 and O3 in *A Orella* depression. Black lines in MCS seismic profiles represent normal faults, indicating an important structural control of the depressions. Note that faults are mainly inclined towards the centre of the depressions.

Fig. 7. a), b) Chirp seismic profiles illustrating the surficial sedimentary configuration at the TZ morphostructural province. Seismic lines display the distribution of the three seismic units identified along the study area (seismic units 1, 2 and 3) and the disposition of the seismic reflectors (S = stratified, Tr = truncated, and T = transparent), as well as the onlap internal terminations. Furthermore, it is also labelled the main geomorphological and sedimentary features, and seismic structures identified: moat, drift deposits, channels, hemi(pelagic) features, structural undulations, structural deformation and erosional surfaces. Black lines represent normal faults affecting the sediments, causing changes in their thickness. Faults also are related to structural undulations and structural deformations; c) correlation of core PC13-3 with the lower limit of seismic unit 1 coincident with an abrupt change at ~ 3.40 m in the grain size distribution; d), e), and f) details of a channel, hemi(pelagic) features, structural deformation and structural undulations, respectively in line K; g) multi-channel seismic profile coincident with the line section f showing the relationship between the deformation of the surficial sedimentary cover with the faults identified at depth. The vertical exaggeration (VE) is indicated in each profile.

Fig. 8. a) Chirp seismic profile showing the presence of filled, partially filled and unfilled pockmarks located within the 1F echo type area. Note the wavy reflectors with V-morphologies delimited by faults associated with gravitational collapses due to fluid escapes; b) enlarged details of the filled pockmarks and c) the partially filled pockmarks, identified at line R. Figure also illustrates the disposition and distribution of the seismic reflectors (S= stratified, Tr = truncated, and T = transparent), as well the identification of the seismic units U3-U1. Black lines represent normal faults, and the vertical exaggeration (VE) is indicated in each profile.

Fig. 9. Three-dimensional figure with a ~19.5X vertical exaggeration (VE) composed by five chirp seismic profiles (Lines M, N, O, P and Q) illustrating the disposition and distribution of the seismic reflectors (Tr = truncated and H= Hyperbolic) within the area surrounding the *Gran Burato* depression and the troughs located at the northwest of this structure. Truncated reflectors are located over the flanks of the depression and troughs, and over the seafloor, which defines an erosional surface. Hyperbolic reflectors are related to the troughs. Moreover, a partially filled pockmark has been identified at line O. Black lines represent normal faults.

Fig. 10. Multi-channel seismic profiles located at the south sector of the TZ morphostructural province; a) line T and b) line S display anticlines structures that configure the fold bulges identified in the geomorphologic map. Blue lines represent normal faults affecting the uppermost sediments within the anticlines structures. It is possible to observe a great structural control over the filled pockmarks identified at line T, and over the structural undulations and troughs located in line S. Note the truncated (Tr) reflectors over the seafloor coincident with the fold bulges. Vertical exaggeration (VE) is indicated in each profile.

Fig. 11. Seafloor ROV observations, accompanied with the location map of the six ROV dives done around the *Gran Burato* depression area: a) ripples with rectilinear crests and accumulation of pteropods into the lows between crest; b) grooves with and without accumulations of pteropods; c) comet marks; d) dense crusts; e) flat surface with some dispersed mounds; and f) accumulation of ferruginous tubes in a flat surface.

Fig. 12. Facies classification of the five studied piston cores extracted from the south sector of the TZ morphostructural province, followed by the optical and radiographical images of each corer. The red star symbols indicate the depth of the radiocarbon dating accompanied by the calibrated age obtained. Note the inverted sequence obtained for PC01 and the hiatus interval coincident with the change of facies in GC16. Also, it is possible to identify a condensed sequence of detrital layers at the top of the cores PC13-3, PCL1-2 and PC06. For more detail about the sedimentary, geochemical and magnetic properties of each core and each facies, see Table 3 and 4, respectively.

Fig. 13. SEM micrographs obtained at different depths illustrating the described facies: a) Ca-rich low-susceptibility/pelagic facies at 400 cm in core PC13-3, composed of foraminifera in a coccolithophorid matrix; b) Ca-rich low-susceptibility/pelagic facies at 260 cm in core PC13-3 with optical magnifying where it is possible to recognise the coccolithophorid matrix; c) Fe-rich high-susceptibility/detrital facies at 54 cm in core PC13-3, composed of foraminifera and terrigenous components of different sizes in a siliciclastic matrix; d) medium Ca and Fe/hemipelagic facies at 370 cm in core PC13-3, formed by foraminifera and terrigenous components in a siliciclastic matrix with variable coccolithophorid content; e) foraminifera-rich sand facies at 50 cm in core PC01, consisting of foraminifera and a small proportion of pteropod shells within in a bioclastic and terrigenous matrix; f) pteropod-rich sand facies at 162 cm in core PC01, composed of foraminifera and a large accumulation of pteropods in a bioclastic and terrigenous matrix; g) low-density sand facies at 8 cm in core GC16; h) high-density silt facies at 19 cm in core GC16. These latter two facies comprises well-preserved foraminifera, accompanied by detrital carbonates and siliciclastic fragments of different sizes, in a well-sorted coccolithophoridae matrix.

Fig. 14. Sedimentation rates obtained for each piston core. Note the general extremely low values, especially during cold stadials.

Fig. 15. a) Schematic representation of the surficial sedimentary cover from a chirp seismic line located at the south sector of the TZ morphostructural province. The intense faulting, folding, and deformation of the upper units indicate strong tectonic control over the most recent sedimentary cover and the geomorphologic features described (e.g. structural undulations). Fault deformation also causes

a change in the sedimentary accommodation space as well as truncate reflectors over the erosional surfaces; b) Schematic cross-section from an MCS seismic line, illustrating the tectono-sedimentary architecture of the domo-like structure located at the south sector of the TZ morphostructural province, based on Ribeiro, (2011). Reactivations of the horst basement and Mesozoic faults during the compressional Cenozoic regimes explain the intense faulting and folding of the post-rift sediments and the uplifted of the marginal platform (Vázquez et al., 2008). This compressional regime is responsible for the tectonic control of the structural undulations, faults deformations, fold bulges, or the giant depressions. The red rectangle indicates the location of the profile section a).

Fig. 16. a) Schematic W-E depth profile and (b) N-S depth profile across the Transitional Zone morphostructural province showing the principal geomorphological features, water-mass structure (ENACW = Eastern North Atlantic Central Water (subpolar); MOW= Mediterranean Outflow Water; LSW= Labrador Sea Water; NADW= North Atlantic Deep Water; LDW= Lower Deep Water) and salinity (orange curve) and temperature (red curve) profiles (taken from <https://odv.awi.de/>). The figure shows that the main water masses acting at the TZ morphostructural province are the MOW, LSW and NADW.

Fig. 17. Schematic representation of the plan view and the N-S sections of the pockmarks-related drifts identified inside the Crater 3 and A Orella depressions. Plan view schemes also indicate the inferred bottom-current paths.

Supplementary data I. Age models tables for each sedimentary piston core used in this study. The age models have been obtained using ^{14}C dates of the five piston cores used in this research, combined with ^{14}C dates and control-points obtained by the correlation of the five cores with the nearby cores MD95-2040 and MD95-2039, located about ~ 245 kilometres south of the study area (de Abreu et al., 2003; Schönfeld et al., 2003).

Supplementary data II. Age models for the PC13-3, PCL1-2, PC06 and GC16 cores, obtained using the OxCal software v4.3.2.

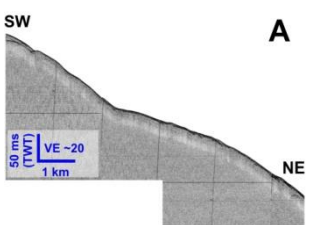
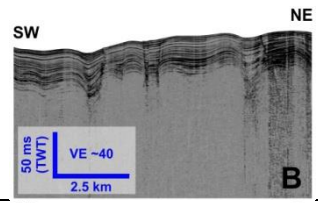
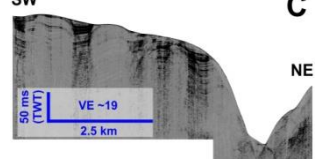
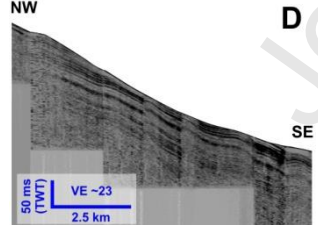
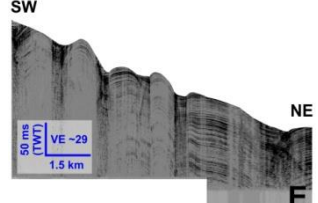
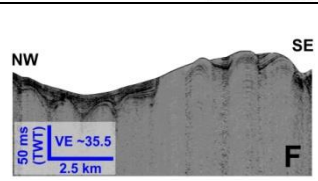
The authors declare no competing interests.

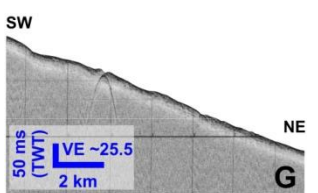
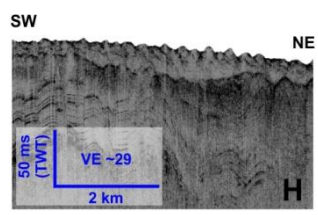
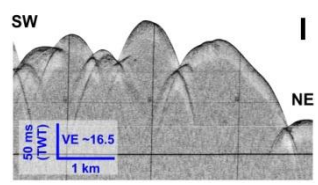
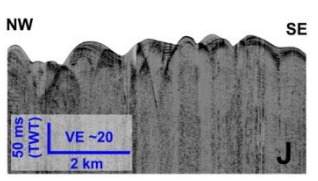
Journal Pre-proof

Table 1. Summary of the piston cores extracted in the study area

Piston core	Latitude (N)	Longitude (W)	Lenght (cm)	Depth (m)	Max. age (cal BP)	Cruise
PC13-3	42° 43' 04.01''	11° 09' 19.43''	428	1,688	~ 172,719	Burato 4240
PCL1-1	42° 38' 13.20''	11° 06' 49.05''	394	1,644	~ 141,190	Burato 4240
PC06	42° 47' 28.98''	10° 46' 16.68''	327	2,827	~ 110,819	Gran Burato 2011
PC01	42° 40' 22.40''	11° 03' 44.90''	179	1,977	~	Gran Burato 2011
GC16	42° 41' 37.70''	11° 02' 31.10''	23	1,734	~ 30,879	MARBANGA

Table 2. Description of the echo types identified. The location of the seismic profiles is indicated in Fig.1.

Echo type	Parametric profile example	Characteristics	Interpretation	Sedimentary processes
Distinct echo				
1A		Distinct continuous sharp bottom echo with absence or with extremely weak sub-bottom reflectors	Erosional surfaces Mounds	Erosive bottom currents processes
1B		Distinct continuous bottom echo and parallel and stratified sub-bottom reflectors	(Hemi)pelagic features Mounded and elongated drifts	(Hemi)pelagic system Countourite system
1C		Distinct continuous bottom echo and undulating, truncated and parallel sub-bottom reflectors	Erosional surfaces	Erosive bottom currents processes
1D		Distinct continuous bottom echo and inclined, truncated and stratified sub-bottom reflectors	Erosional surfaces	Erosive bottom currents processes
1E		Weak continuous bottom echo and truncated and parallel sub-bottom reflectors	Channels Troughs Erosional surfaces	Erosive bottom currents processes
1F		Distinct continuous bottom echo with undulating, parallel, truncated, discordant and outcropping sub-bottom reflectors	Pockmarks Erosional surfaces	Fluids escapes Erosive bottom currents processes

1G		Weak distinct bottom echo with high reflectivity sedimentary layer on an irregular and not defined base	Mass transport deposits	Depositional processes
Wavy echo				
2A		Wavy irregular bottom echo with transparent fill over an irregular base, followed by intermittent transparent layers and by parallel, undulated and discontinuous sub-bottom reflectors not concordant with the seafloor	Sediment waves	Erosive bottom currents processes
Hyperbolic echo				
3A		Bottom echo with irregular and overlapping hyperbolas without sub-bottom reflectors	Channels Gullies Mounds Scarps Structural highs	Bottom-current/ gravitationally erosive processes Abrupt topographic changes Basement outcrop
3B		Irregular overlapping hyperbolas with truncated, concordant or absence of sub-bottom reflectors	Channels Scarps	Erosive mass-movement processes Erosive bottom currents processes

Journal Pre-proof

Table 3. General sediments properties for the cores

Core	Parameter	% Sand	% Silt	% Clay	MGS (μm)	Sorting (μm)	MS (10 ⁻⁵ SD)	Fe/Ca	Ti/Ca	Si/Sr	Fe (p.a.)	Ti (p.a.)	Ca (p.a.)	Ba (p.a.)	Mn (p.a.)	R	G	B	GL
PC13-3	Mean	45.53	39.52	14.95	88.99	67.04	6.07	0.1327	0.0029	0.0209	17.498.1	375.6	163,653.77	43.48	226.1	23	20	17	33,561.53
	S.D.	32.42	21.17	12.44	68.79	43.05	6.44	0.1509	0.0040	0.0184	11.834.6	334.0	39,118.46	22.40	159.0	14	23	39	108.30
PCL1-2	Mean	74.91	20.08	5.01	19.12	12.03	3.89	0.0740	0.0012	0.0068	9.792.13	149.5	138,702.73	44.17	147.0	21	18	12	33,058.25
	S.D.	26.54	20.06	6.60	87.87	57.75	9.85	0.0486	0.0014	0.0056	4.312.55	128.0	12,335.16	21.57	98.20	17	22	3	52.10
PC06	Mean	33.81	50.93	15.26	68.30	92.75	10.92	0.9431	0.0023	0.0037	35.57.2	8740.3	1,866.14	68.28	204.2	16	49	13	33,837.67
	S.D.	13.87	10.15	4.57	27.01	22.38	12.64	1.2725	0.0031	0.0035	22.661	60.1	30,866.65	29.76	114.7	31	28	24	223.27
PC01	Mean	88.44	8.94	2.63	26.85	20.02	6.01	0.1228	0.0024	0.0011	1.415.8	241.9	106,267.19	36.22	173.0	10	35	95	33,913.22
	S.D.	6.30	4.72	1.64	51.13	10.33	9.14	0.0924	0.0053	0.003	7.390.89	99.28	14,990.33	15.03	547.5	15	15	11	277.08
GC16	Mean	44.01	36.94	19.05	97.30	106.7	6.82	0.0842	0.0009	0.004	9.617.05	217.4	117,679.76	24.12	260.5	16	44	10	33,630.46
	S.D.	15.11	8.54	7.56	58.88	48.98	12.16	0.0272	0.0007	0.0029	2.535.64	68.70	13,730.72	7.21	125.2	29	28	29	156.72

Table 4. Statistical values from the variables used for the statistical described of the cores

Core	Facies	Parameter	% Sand	% Silt	% Clay	MS (10 ⁻⁵ SD)	Fe/Ca	Ti/Ca	Si/Sr	Fe (p.a.)	Ti (p.a.)	Ca (p.a.)	Ba (p.a.)	Mn (p.a.)	R	G	B	GL	MS (μm)	Sorting (μm)
PC13-3	Pelagic	Mean	45.67	38.83	15.50	3.30	0.0730	0.0015	0.0144	12.925.50	259.75	183,418.82	37.00	184.97	22	21	18	33,554.89	94.30	70.10
		S.D.	31.28	19.79	12.63	2.29	0.0304	0.0008	0.0065	4.022.19	108.60	22,568.96	12.72	94.39	33	18	33	105.41	69.98	43.88

	Hemipelagic	Mean	42.93	42.32	14.74	8.42	0.1415	0.0027	0.0190	17,055.27	325.55	132,087.38	40.21	227.00	23	20	15	33,589.19	75.24	56.04
		S.D.	33.81	23.10	11.12	6.52	0.0691	0.0018	0.0125	5,105.03	169.33	34,767.78	16.44	132.22	12	18	11	131.13	55.05	35.33
	Detrital	Mean	53.17	36.86	9.98	16.58	0.4229	0.0105	0.0566	41,350.74	1,036.47	109,064.11	81.13	433.67	25	17	11	33,555.15	91.51	73.10
		S.D.	16.10	11.83	4.36	7.43	0.2395	0.0066	0.0248	16,093.39	479.79	27,804.81	30.28	261.34	18	15	17	74.973	33.52	19.35
	Pelagic	Mean	81.44	15.14	3.43	0.91	0.0600	0.0008	0.0052	8,432.13	110.06	142,829.79	36.94	128.33	21	18	12	33,072.15	212.83	133.97
		S.D.	18.71	14.04	4.73	2.77	0.0202	0.0005	0.0029	2,375.20	63.12	8,936.85	16.79	92.60	13	81	11	48.803	72.15	51.85
PCL 1-2	Hemipelagic	Mean	31.61	52.75	15.65	8.01	0.0990	0.0018	0.0081	12,354.85	226.73	125,745.59	64.52	248.22	19	17	11	32,999.24	56.16	52.13
		S.D.	21.57	16.33	5.60	4.94	0.0196	0.0005	0.0036	2,030.18	53.08	7,444.69	9.25	73.08	11	91	88	12.893	38.38	29.07
	Detrital	Mean	71.97	22.19	5.84	20.35	0.1412	0.0030	0.0166	16,151.15	330.56	125,665.79	70.88	155.86	19	17	13	33,030.26	171.04	109.86
		S.D.	22.64	16.39	6.35	21.03	0.1059	0.0031	0.0097	7,883.64	255.56	16,328.11	24.88	78.12	21	17	18	42.941	73.12	32.86
	Pelagic	Mean	36.32	48.10	15.57	4.49	0.2854	0.0068	0.0169	22,092.86	515.27	90,960.11	52.88	155.91	17	16	12	33,808.30	71.55	96.02
		S.D.	12.94	9.18	4.61	3.83	0.2257	0.0063	0.0121	10,816.33	211.01	18,119.64	18.75	106.66	25	22	20	203.89	23.15	15.34
PCO 6	Hemipelagic	Mean	37.13	48.46	14.41	17.51	1.2927	0.0321	0.0497	17,734.7	1,203.72	49,240.18	102.62	253.53	14	13	9	33,868.50	77.75	100.15
		S.D.	14.23	9.63	4.91	7.76	0.8669	0.0119	0.0682	17,581.9	406.87	20,417.47	14.18	73.31	12	11	7	78.301	30.12	24.43
	Detrital	Mean	24.96	59.09	15.96	24.97	2.6774	0.0682	0.0800	67,028.00	1,733.09	31,374.40	88.33	313.16	21	21	8	33,903.10	51.60	78.60
		S.D.	8.44	6.43	2.58	17.64	1.6337	0.0388	0.0345	15,057.21	327.70	11,235.05	31.69	62.73	13	11	6	319.66	15.86	17.47
	Sand-rich-foraminifera	Mean	90.44	7.31	2.24	8.08	0.1302	0.0024	0.0123	13,952.80	261.62	111,377.69	31.53	220.23	15	13	9	33,811.87	269.68	182.59
		S.D.	1.41	1.14	0.38	15.22	0.0906	0.0010	0.0086	7,583.19	70.42	9,055.72	8.17	647.72	16	11	10	171.50	45.57	101.18
PCO 1	Sand-rich-pteropods	Mean	83.76	12.84	3.39	3.09	0.09712	0.0015	0.0064	6,974.80	149.88	99,024.65	42.28	51.82	14	13	7	34,239.70	274.67	262.66
		S.D.	8.48	4.09	2.40	3.29	0.0252	0.0007	0.0037	2,443.46	59.06	15,602.75	17.70	21.02	14	13	9	264.85	51.39	59.44
	Detrital	Mean	79.53	11.45	5.02	5.69	0.3056	0.0072	0.0233	19,539.40	464.87	66,307.50	76.27	122.02	14	13	9	33,632.88	239.14	230.87
		S.D.	2.04	1.41	0.65	4.22	0.1033	0.0025	0.0049	5,622.24	144.35	9,685.47	10.36	34.66	44	44	4	103.06	25.65	38.65
GC 16	Low-density	Mean	51.30	34.71	13.99	7.15	0.0990	0.0021	0.0103	10,900.76	231.97	111,222.63	27.07	298.17	14	12	8	33,706.40	121.53	120.96
		S.D.	11.20	7.55	3.92	4.81	0.0143	0.0004	0.0016	1,150.81	37.38	11,540.16	6.28	102.16	88	88	4	143.26	47.48	41.16
	High-density	Mean	31.39	41.75	26.85	7.23	0.0601	0.0016	0.0078	7,523.38	193.84	128,211.04	19.31	199.21	19	19	4	33,506.61	51.86	70.06
		S.D.	3.88	2.11	2.01	17.30	0.0261	0.0009	0.0038	2,777.70	96.48	10,022.22	5.94	135.47	11	11	1	80.177	10.05	11.51

- Surficial sediments are affected by structural features suggesting a tectonic activity still active until recent times.
- Topographic and oceanographic factors induce an intensification of the bottom-hugging currents with their concomitant erosion capacity.
- Erosional activity results in coarser grain-size facies than expected in an offshore source-to-sink sedimentary system.
- A new kind of contourite associated with giant depressions has been defined: the pockmarks-related drift.